J. Fluid Mech. (1997), *vol.* 332, *pp.* 295–339

Primary and secondary instabilities in the wake of a cylinder with free ends

By CHRISTOPHE DAUCHY[1], JAN DUŠEK[2] AND PHILIPPE FRAUNIÉ[3]

[1]Institut de Recherche sur les Phénomènes Hors Equilibre, 12, Avenue du Général Leclerc, 13003 Marseille, France
e-mail: dauchy@marius.univ-mrs.fr

[2]Institut de Mécanique des Fluides de Strasbourg, 2, rue Boussingault, 67000 Strasbourg, France
e-mail: dusek@imf.u-strasbg.fr

[3]LSEET, Université de Toulon et du Var, B. P. 132, 83957 La Garde, Cedex, France
e-mail: fraunie@lseet.univ-tln.fr

(Received 12 February 1996 and in revised form 18 September 1996)

The wake of a finite cylinder with free ends and an aspect ratio of 21.4 is simulated in three-dimensions and analysed theoretically. Close to the primary-instability threshold, the flow is shown to settle on a limit cycle with a uniform frequency throughout the flow-field. About 20% above the primary-instability threshold, a secondary instability sets in and the limit cycle becomes unstable. The new attractor of the flow can be identified as a limit T^2-torus characterized by two incommensurate frequencies. One of them is shown to evolve continuously from the primary-instability frequency, the other one, about 17 times smaller near the secondary-instability threshold, generates a slow modulation of the oscillations in the wake. The limit cycle and the limit torus are described in terms of their Fourier expansion and the spatial distribution of the most relevant Fourier components is investigated. The theoretical analysis and numerical results given shed some light on the mechanisms underlying a number of known but not satisfactorily explained three-dimensional effects in wakes of finite cylinders such as the ambiguity in the dominant Strouhal frequency, the existence of zones with different frequencies spanwise in the wake, the discreteness of coexisting frequencies observed in the wake as well as the spatial uniformity of the beating period. They moreover explain the Reynolds number variation of these effects and identify the recirculation around the cylinder ends as basically responsible for the onset of the secondary instability. The results are compared to the case of a cylinder with aspect ratio of 10.7 to determine the basic trends in aspect ratio dependence. It is shown that qualitatively the same behaviour is obtained, but that the secondary-instability threshold is shifted significantly upward to about twice the primary-instability threshold. Simulations of the wake of a finite NACA wing with incidence show that the form of the cross-section plays a minor role.

1. Introduction

1.1. *Problems of investigation of the Bénard–von Kármán instability*

The intriguing regularity of the cylinder wake has attracted the attention of numerous researchers for over hundred years since the phenomenon was first described by

Strouhal. The ideal configuration giving rise to the regular vortex shedding is that of the infinite circular cylinder. The Bénard–von Kármán instability, which is at its origin, conserves the translational invariance along the cylinder axis reducing the flow to two dimensions and making the numerical description of the wake of an infinite cylinder particularly easy. Two-dimensional simulations (e.g. Braza, Chassaing & Ha Minh 1986; Karniadakis & Triantafyllou 1989; Dušek, Le Gal & Fraunie 1994*b*) not only reproduced accurately the basic flow characteristics obtained experimentally such as the Strouhal number and the critical Reynolds number, but also led to a detailed explanation of the nonlinear mechanisms governing the instability development (Carte, Dušek & Fraunie 1996) and a detailed description of its spatial characteristics (Dušek 1996).

The realization of an experimental set-up providing strictly two-dimensional vortex shedding has been, in contrast, a difficult challenge for generations of experimenters. The measurements of Roshko (1954) were carried out on cylinders with an extremely high aspect ratio. Subsequent experimental attempts to confirm Roshko's phenomenological law concerning the Reynolds number dependence of the vortex shedding frequency brought evidence of the complicated nature of wakes of real finite cylinders making the interpretation of the experimental results difficult (Tritton 1959). The progress in experimental techniques shed light on the three-dimensional end effects and brought them under control. Gaster (1971), Gerich & Eckelmann (1982) and Eisenlohr & Eckelmann (1989) introduced end plates fixed to the cylinder to control the end effects. Other alternatives consist of placing transverse cylinders upstream of the main one (Hammache & Gharib 1989) or short coaxial hollow cylinders at the ends (Eisenlohr & Eckelmann 1989) or of investigating configurations without end effects such as rings normal to the flow direction (Leweke & Provansal 1995).

The progress in experimental techniques allowed stable parallel vortex shedding to be achieved in a wide interval of Reynolds numbers between the instability threshold at $Re = 46$ and the onset of the transition to three-dimensionality and turbulence at $Re \approx 180$ with reasonable aspect ratios of cylinders. Very fine experiments and accurate data (Williamson 1989, 1992 and Williamson & Prasad 1993) could thus be obtained. The perfection of the experimental two-dimensionality achieved is confirmed by the very good agreement between experiments and numerical simulations (see Williamson 1989 and Williamson & Prasad 1993 and the numerical data in Dušek *et al.* 1994*b* and Dušek 1996). The success in controlling the three-dimensional effects in the cylinder wake had, however, a negative impact on the effort to understand them.

1.2. *Present trends of study of three-dimensional effects*

In contrast to earlier experimental papers (Tritton 1959; Gaster 1969, 1971; Gerich & Eckelmann 1982 and Eisenlohr & Eckelmann 1989), recent work is mostly concerned with the onset of three-dimensionality in an infinite (two-dimensional) configuration, the techniques of elimination of three-dimensional end effects being used in experimental set-ups. This research seems to have been triggered by Sreenivasan (1985) who found the Ruelle–Takens–Newhouse (Ruelle & Takens 1971; Newhouse, Ruelle & Takens 1978) scenario of transition in the cylinder wake for very low Reynolds numbers. The observation of Sreenivasan was attributed later by Van Atta & Gharib (1987) to an aeroelastic effect, but other physical or numerical effects yield the same scenario (e.g. Olinger 1990; Abarbanel *et al.* 1991; Williamson & Prasad 1993). Sreenivasan's work also stimulated a substantial numerical (Karniadakis & Triantafyllou 1992; Noack, König & Eckelmann 1993; Noack & Eckelmann 1994; Dušek, Fraunie & Seror 1994*b* and Barkley & Henderson 1996) and experimental (Williamson 1992; Albarède & Provansal 1995; Leweke & Provansal 1995) effort to investigate the transition of the cylinder wake (or the wake of a thin torus) to turbulence. The contradictions characterizing these works can be explained by the different configurations considered to simulate the infinite geometry. The numerical results based on simulations of the cylinder wake in spanwise periodic configurations predict, systematically, a period doubling at the transition to three-dimensionality (Karniadakis & Triantafyllou 1992; Dušek *et al.* 1994*a*). The experimental results give, rather, evidence of a low incommensurate frequency appearing almost from the onset of vortex shedding near the end of finite cylinders. It has been clearly recognized that these effects are due to the presence of the cylinder ends (Gerich & Eckelmann 1982; König, Eisenlohr & Eckelmann 1990, 1992; Brede *et al.* 1994). However, even in experiments where the end effects have been suppressed by the experimental set-up a lower frequency still sets in at Reynolds numbers at which the transition to turbulence is observed (at $Re = 180$ in Williamson 1992 for a long cylinder and at about $Re = 200$ in Leweke & Provansal 1995 for a torus). Among the cited papers, the only 'perfectly infinite' cylinder configuration is that of Noack *et al.* (1993), Noack & Eckelmann (1994) and Barkley & Henderson (1996). A numerical instability analysis shows unambiguously that the onset of three-dimensionality in the infinite cylinder wake is due to a real bifurcation, i.e. that no new frequency arises. The bifurcation yields translational symmetry breaking in the spanwise direction. Two different modes have been identified experimentally and numerically as the most unstable at the transition to three-dimensionality in the infinite configuration: an 'A-mode' characterized by a critical wavelength of about 4 (Williamson 1992; Barkley & Henderson 1996) and a 'C-mode' with about half that wavelength (Noack *et al.* 1993) the discrepancy being explainable by different level of spatial resolution used in the cited numerical papers (Zhang *et al.* 1995). The role of end effects seems, however, to prevail in the transition of wakes of bodies with finite geometries (Zhang *et al.* 1995).

1.3. *Three-dimensional effects in wakes of finite objects at low Reynolds number*

Wakes forced with frequencies incommensurate with the natural vortex shedding are known to present a strong lock-in trend making the natural frequency disappear in favour of a rational frequency ratio. For the description of lock-in effects in wakes of oscillating cylinders in terms of nonlinear dynamics, see Olinger & Sreenivasan (1988) and Olinger (1990). Similarly the limit cycle character of the primary instability of an unforced infinite cylinder wake has been attributed (Dušek *et al.* 1994*b*) to the trend of the vortex shedding frequency to be uniform in space.

In unforced wakes of finite cylinders the presence of two distinct frequencies is very common and the lock-in effects seem to be absent. Such behaviour, characterized by two distinct frequencies at the same location of the wake yielding modulation (beatings) in signals of velocities and of different dominant frequencies in various regions of three-dimensional wakes, were first reported by Tritton (1959), Gaster (1969, 1971) and Gerich & Eckelmann (1982) for Reynolds numbers lying significantly below the transition threshold. Tritton (1959) carried out hot-wire measurements at different stations downstream of the cylinder and at several distances off the symmetry plane containing the cylinder axis but did not study systematically the spanwise variations of the velocity oscillations. He found a discontinuity in the Strouhal *vs.* Reynolds number curve that was explained by the switching from one dominant frequency (a 'low speed mode') to a slightly lower one (a 'high speed mode'). The difference of the modes was attributed to a different mechanism of the vortex shedding. The low-speed mode was believed to originate in the wake instability whereas the high-speed mode was interpreted as a result of shedding of attached eddies off the cylinder wall. The transition between them was characterized by marked, often periodic, beatings. The period of the beatings was found to be about 6 to 14 times that of the period of basic oscillations. Strongly three-dimensional deformations of vortex lines were pointed out. A similar transition between modes with different frequencies was described by Berger (1964).

An interesting study of the relation between a three-dimensional geometry and the spatial variations of the vortex shedding frequency was given in Gaster (1969). It was assumed that the vortex shedding frequency may vary spanwise due to variations of the local Reynolds number of the obstacle. Such variations are always present at least near the ends whether the latter are tapered to make the variation more progressive or not. To make the argument more explicit, Gaster measured the wake of a slender cone for which the local Reynolds number varied spanwise proportionally to its length. Very clean periodic beatings were observed. The frequency of beatings was found to increase proportionally to the Reynolds number based on the cone length and to be the same throughout the flow (independently of the spanwise position of the probe), i.e. as stated in Gaster (1969): “the low-frequency modulation is not a local phenomenon”. In contrast, the rapid vortex shedding frequency was observed to obey Roshko’s law (Roshko 1954) if the local Strouhal number (based on the local cone diameter) was plotted versus the local Reynolds number along the span of the cone. The question may arise how the ‘local’ frequency was determined in the presence of beatings. As specified in Gaster (1969), this was done by taking the frequency near the maxima of the beatings. A theoretical model giving an explanation of the beatings and of the spanwise ‘locality’ of the vortex shedding frequency as a result of three-dimensional effects of the spanwise variation of the local Reynolds number was presented. To confirm this conclusion, the behaviour of the wake of a cone was, moreover, compared to that of a perfect cylinder in the same experimental conditions and it was shown that no beatings could be detected in a wide range of Reynolds number in this case.

The experiments of Tritton (1959) and Gaster (1969) triggered a controversy concerning the interpretation of the origin of the observed beatings (or irregularities) in the vortex shedding (Tritton 1971; Gaster 1971). It lead Gaster to refine his experiment and to present the following further interesting conclusions (Gaster 1971). Regular periodic shedding was found to occur in several cells (up to four) with jumps in frequency between neighbouring cells for a very slightly tapered cylinder. The beatings observed in the transition regions between neighbouring cells corresponded precisely to the difference of the frequencies of the neighbouring cells. A similar pattern resulted in the flow around a perfect cylinder placed in a flow with a slight spanwise shear. When the flow velocity was varied the cells were observed to move along the span. As a result, slight fluctuations of the flow velocity occasioned displacements of the cells on a very gradually tapered cylinder also and the sensitivity of the pattern to the flow fluctuations was the higher the more gradual the spanwise variation of the diameter was. The wandering of the cells could be stopped by placing end plates on the cylinder.

The influence of end effects on the vortex shedding was further analysed by Gerich & Eckelmann (1982). They showed that, although a continuous law governing the Strouhal *vs.* Reynolds number dependence could be recovered using end plates and although the beatings could thus be eliminated from the central zone of the cylinder span, a zone, called the affected zone, characterized by a lower frequency is always present near the ends of the cylinder whether these ends are free or delimited by end plates. A strong ‘lock-in’ effect allowing only two frequencies in the wake was shown in the whole affected zone where the lower frequency was also uniform. In the region of transition between the central and the affected zone marked beatings could be observed. It is important to note that Gerich & Eckelmann did not find the onset of beatings to coincide with the onset of the vortex shedding that occurred in their configuration at $Re_1 \approx 50$. A narrow interval $Re_1 < Re < Re_2$ was found for which only one vortex shedding frequency could be found in the wake. The critical Reynolds number Re_2 at which the beatings were observed to set in was about 57. The length of the affected zone was measured at $Re = 150$. At this Reynolds number, it was found to extend about 10 cylinder diameters from the free ends or from large end plates. The ratio of the frequency of basic oscillations and of the beatings, which is indicative of the frequency difference between the central and the end zone, was found to decrease continuously from about 11 at $Re = 57$ to 6 at $Re = 154$. For small aspect ratios, i.e. for cylinders having a spanwise length smaller than the overall length of both affected zones the beatings were observed to disappear, but the vortex shedding frequency lay between that of the affected and central zones and was thus lower than the two-dimensional one.

Altering the end zones of the cylinder appeared to be an efficient means of vortex shedding control. Reduction of the cylinder diameter at the ends leads to a lower vortex shedding frequency. Conversely, the frequency can be increased by increasing the local diameter near the ends. In this way the end effects can be compensated. A single frequency corresponding exactly to the two-dimensional value could be obtained by placing two coaxial hollow cylinders of about twice the diameter of the principal one along its ends (Eisenlohr & Eckelmann 1989). The analysis of three-dimensional effects could be used to explain definitively (König *et al.* 1990) the discontinuity in the Strouhal *vs.* Reynolds curve observed by Tritton (1959). It was recognized that the geometry of the cylinder ends, the aspect ratio and the distance from the ends govern the character of the recorded velocity signal.

Later papers (König, Noack & Eckelmann 1993; Brede *et al.* 1994) stress the discrete nature of the vortex shedding frequencies found in the cylinder wake. The frequencies appear to vary with a well-defined step from one ‘shedding cell’ to another and are reminiscent of quantum mechanical energy spectra. A still finer frequency spectrum is found in a slender cone wake, showing clearly that the spatial frequency variation of Gaster (1969) is, actually, also discrete (König 1993).

The cited experimental results prove that the three-dimensional geometry of the wake of finite objects leads to special effects that give rise to some of basic questions. The most important problem is related to the presence of frequencies varying in space in a low Reynolds number flow in which strong ‘lock in’ effects are known to predominate. Whether the vortex shedding frequency varies continuously along the span of the obstacle as claimed by Gaster (1969) or stepwise as in Gaster (1971) and Gerich & Eckelmann (1982) and later papers cited above, the interpretation in terms of ‘local’ Reynolds numbers or separated zones is in contradiction to the global character of the wake confirmed by the frequencies of the modulation which are uniform in space. It should be made clear whether separate zones with incommensurate frequencies can exist in a laminar wake and their origin should be explained.

1.4. *Progress in understanding of the primary instability mechanisms*

For low Reynolds number flows instability theory accounts well for all observed phenomena. The vortex shedding in the wake of an infinite cylinder has been many times, and with an increasing degree of sophistication, investigated theoretically in terms of linear instability theory with the objective to describe its onset and predict its frequency (see e.g. Mattingly & Criminale 1972 as an example of early work based on the parallel flow instability theory, the fully two-dimensional linear theory of Jackson 1987 or the review of Huerre & Monkewitz 1990 for other references). The effort to derive a theoretical framework explaining the three-dimensional phenomena in low Reynolds number wakes (near the primary instability threshold) has so far been limited to semi-phenomenological models focusing only to some partial aspects of the problem (Gaster 1969; Leweke & Provansal 1995; Albarède & Provansal 1995).

In a recent paper (Dušek *et al.* 1994*b*) a fully nonlinear approach based on basic concepts of the theory of dissipative dynamical systems was applied to give an exact theory of the two-dimensional wake based solely on the Navier–Stokes equations. In this framework, it can be said that the flow field described mathematically as a steady solution of the Navier–Stokes equations undergoes a Hopf bifurcation at $Re_1 \approx 46$. Above this critical Reynolds number value the steady flow solution becomes unstable (see also the experimental study of Strykowski & Sreenivasan 1990). An infinitesimal perturbation deviates the flow from its steady state and oscillations characterizing the onset of instability appear. Linear instability theory predicts the amplification rate and the frequency of oscillations to be uniform in space. This result is a trivial consequence of the fact that the amplification rate and the linear vortex shedding frequency are, respectively, the real and the imaginary part of the unstable eigenvalue of the linear eigenvalue problem. The amplification was shown (Sreenivasan, Strykowski & Olinger 1987, Mathis, Provansal & Boyer 1987) to follow qualitatively the Landau model (Landau & Lifshitz 1959) to reach a state, called saturation, at which the amplitudes of oscillations become steady. This asymptotic state of the flow has been identified (Dušek *et al.* 1994*b*), by analysing numerical simulations, as a limit cycle in the functional sense. It means that all the flow characteristics, such as velocities and pressure, oscillate with a period that is uniform in space. This limit cycle, as well as any limit cycle known in finite-dimensional systems, can be represented in terms of a Fourier decomposition into harmonics, the latter being in this case complex functions in space. The harmonics, describing the envelopes and phases of oscillations throughout the space, have been shown to be non-zero in the whole space (Dušek *et al.* 1994*b*) (except sets of zero measure), i.e. in particular upstream of the obstacle as well as downstream, and to have a space structure giving rise to the typical plane wave vortex shedding in the far wake and reflecting the symmetry of the geometrical configuration (Dušek 1996). The nonlinear mechanisms of the transfer of energy from the mean flow to the fundamental, back to the mean flow and up to higher harmonics could be analysed (Carte *et al.* 1996) by means of a specially designed numerical method (Carte, Dušek & Fraunie 1995). This analysis demonstrated the relevance and practical importance of the dynamical system viewpoint.

1.5. *Objectives of the present study*

The purpose of the present paper is to extend the so far two-dimensional analysis of an infinite cylinder wake to wakes with three-dimensional effects. The method of investigation is based on a direct numerical solution of the Navier–Stokes equations and its subsequent theoretical analysis. In view of existing experimental data and for numerical convenience, cylinders with free ends and moderate but not too small aspect ratios have been chosen. The geometrical configurations, the numerical method and numerical trade-offs of the simulations are presented in §2. The wake of the investigated objects is shown to undergo a primary and a secondary bifurcation at fairly low Reynolds numbers, both bifurcations being of Hopf type. In §3 the primary instability is investigated fully in three dimensions as a limit cycle of the three-dimensional flow field. In §§4 and 5 the onset of the secondary instability is described in terms of an instability of the limit cycle and a transition to a limit T^2-torus and a conceptually simple but exact theoretical framework is given. In §6 some basic characteristics of the limit torus introduced in §5 are presented. The influence of aspect ratio of the cylinder on the described behaviour is analyzed in §7. The theoretical implications and perspectives are discussed in §8.

2. Numerical method

2.1. *Simulated configurations*

The numerical simulations have been carried out using the Nekton† three-dimensional spectral element (Patera 1984) Navier–Stokes solver. The spectral element method seemed most appropriate because of its capability to treat complex geometries and its lack of numerical diffusion. Four geometrical configurations have been considered:

(i) a full circular cylinder of aspect ratio 21.4 (figure 1*a*),

(ii) a half-cylinder mimicking the full configuration of the same aspect ratio using a numerical symmetry condition with respect to the symmetry plane normal to the cylinder axis (figure 1*a*),

(iii) a full cylinder of aspect ratio 10.7 and

(iv) a half-NACA 0012 wing of aspect ratio 12 with a 34° incidence.

The results concerning the NACA wing will, however, be only briefly mentioned in this paper (for more details see Dauchy 1995), only to show that wakes of more general, non-symmetrical, objects present the same behaviour as the wake of a circular cylinder. The diameter of the cylinder and the chord and incidence of the NACA wing were chosen so that their effective cross-sections were the same. Common length units were chosen for the cylinder and the NACA wing so that the chord length of the NACA profile was $c = 1$ and the cylinder diameter $d = 0.56$.

Because of the necessity to capture more complex dynamics than that of the periodic primary instability of the cylinder wake relatively long runs were required. The length of the runs added to the increased complexity related to the three-dimensional configuration. Special attention had thus to be paid to keeping the computing costs within reasonable limits. The full configuration was used only for testing the physical relevance of the results obtained in the half-domain with a symmetry plane.

2.2. *Spectral element mesh*

The mesh used for the half-cylinder simulating the L/d=21.4 geometry is represented in figure 1(*b*). In the streamwise direction, it extends from about 4 cylinder diameters upstream to 13.8 diameters downstream of the cylinder axis. (The overall length of the domain is 10 units, i.e. about 18 cylinder diameters.) In the transverse direction, the lateral boundaries are placed at 3.6 diameters from the cylinder axis. In the spanwise direction, the symmetry plane coincides with the $z = 0$ plane. The spanwise width of the domain is 14.3 cylinder diameters, the cylinder half-length being 10.7 diameters. As a result, about 3.6 diameters are left between the cylinder tip and the domain boundary. The ‘infinity’ of the domain is simulated by a uniform free-stream velocity ($U = 1, V = 0, W = 0$) condition in the planes limiting the domain

---

† Copyright © 1991 by creare.x, Inc., Hanover, New Hampshire, USA, Nekton is a registered trademark of Nektonics, Inc. and the Massachusetts Institute of Technology.

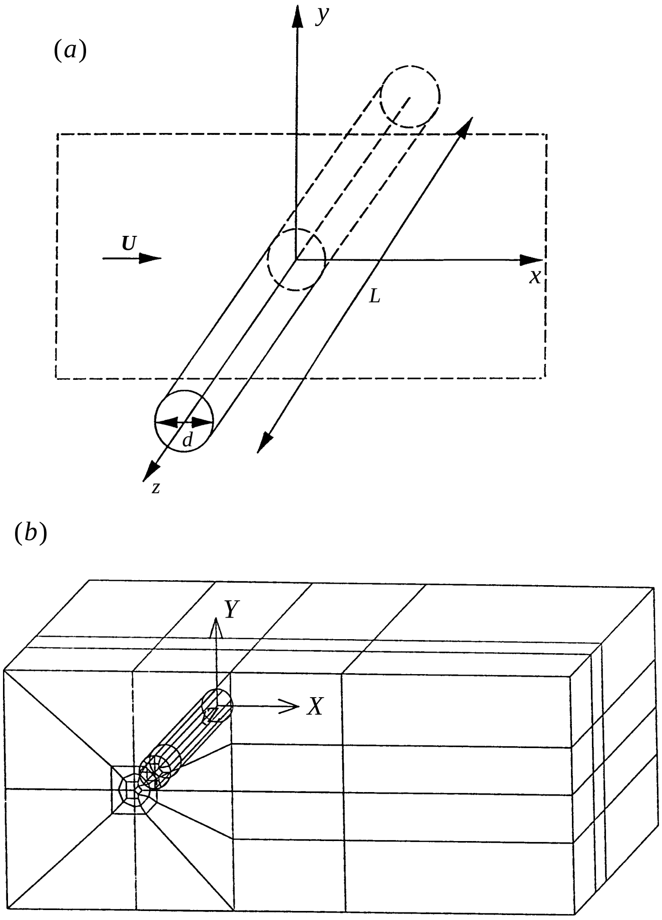

Figure 1. (*a*) The configuration of the full and of the half-cylinder of diameter $d = 0.56$ and full length $L = 12$ or $L = 6$ (aspect ratio 21.4 and 10.7, respectively). The orientation of axes is also represented: x-axis parallel to the inflow velocity $\boldsymbol{U}$, z-axis oriented along the cylinder axes and y-axis normal to the plane $(\boldsymbol{U}, Oz)$. The origin is placed at the centre of the intersection of the cylinder with the symmetry plane xOy. (*b*) Macroelement mesh for the half-cylinder. The length unit is chosen so that the cylinder diameter is $d = 0.56$ and its half-length $L/2 = 6$.

in the transverse and in the spanwise direction. At the inflow, the same uniform free-stream velocity condition is imposed. The outflow conditions used are those supplied with the code†. They consist of setting the stresses at the outflow equal to zero. It has been verified that not only is the volume well conserved but the vortex structures appear to leave the domain fairly freely and without appreciable reflections. In figure 1 only macro-elements are represented. They are distributed in three layers of thickness equal to 8.9, 1.8 and 3.6 diameters and their total number is 99 for this configuration. Each element contains six collocation points of the pseudo-spectral interpolation polynomials (Patera 1984) in each space direction, i.e. 216 altogether. Taking into account the boundary conditions and continuity conditions at element interfaces the total number of effective degrees of freedom of the mesh is thus roughly 10 000 per discretized variable (velocity component, pressure). The

† Nekton, User's Guide.

time discretization was based on the semi-implicit first-order time-splitting method of Korczak & Patera 1986 (described also in Karniadakis & Triantafyllou 1989). The numerical stability requirements and the existence of very small elements near the cylinder tip limited the time step to a value corresponding roughly to 1800 time steps per Strouhal period. The CPU time of simulation of one Strouhal period is a good indicator of the computing costs of simulation of the wake dynamics, typically one to two hundred Strouhal periods being necessary to settle to the investigated attractor and to determine its characteristics. For the half-cylinder configuration with 99 spectral elements the CPU time was about 2.2 h per Strouhal period on a machine with an estimated real performance of about 40 Mflops (DEC Alpha 2100 4/250), double the time was needed for the complete 198 configuration. Typically two or more weeks were needed to investigate the dynamics at one Reynolds number value.

2.3. *Numerical trade-offs*

To reach perfect quantitative agreement with a real configuration would have required significantly higher computing costs. In two dimensions, a mesh that allows a really good numerical convergence of the spatial discretization and a better than 1% agreement with experimental values of the principal characteristics of the cylinder wake to be reached is given in Dušek *et al.* (1994*b*). The two-dimensional projection of the mesh used here corresponds roughly to the central zone of the mesh in figure 1 of Dušek *et al.* (1994*b*), except that the number of collocation points per element and per space direction is only 6 instead of 14. In spite of the drastic reduction of the number of collocation points per space direction and of the mesh extension, the three-dimensional mesh of the half-domain has almost twice as many effective degrees of freedom as the very accurate two-dimensional mesh of Dušek *et al.* (1994*b*). Owing to the small elements near the cylinder end mentioned above the time step of the present three-dimensional simulation was only slightly longer than in the two-dimensional case (1800 time steps instead of 2500 per Strouhal period). After the limit cycle was reached, the whole two-dimensional wake dynamics could be captured, in principle, within one period of simulation (the computation of the transients due to the instability amplification was done with a lower resolution) whereas the investigation of the more complex dynamics of the three-dimensional wake necessitated, typically, a simulation of one to two hundred of Strouhal periods. As a result, in spite of the substantial trade-offs in the space discretization accuracy of the three-dimensional mesh, the present study was, computationally, considerably more expensive than in the two-dimensional case. The mesh represented in figure 1, nevertheless, brought the computing costs within reasonable limits and enabled the simulations to be carried out on current workstations.

The effects of the numerical trade-offs could be roughly estimated and assurance of the qualitative relevance of the results could be obtained. A detailed analysis of the relation between the numerical errors of the spectral element method and the most important characteristics of the Bénard–von Kármán instability (Dušek & Fraunié 1993) has shown that a qualitatively correct picture of the unstable two-dimensional wake could be captured with quite a low resolution and on a limited two-dimensional domain of the type obtained as a two-dimensional projection of the present three-dimensional mesh. Actually, a simulation with only 20 spectral elements having as few as 6 collocation points in each space direction has been shown to yield a qualitatively correct wake.

The following discretization parameters have been tested in two dimensions: the distribution of elements, the number of collocation points per element and space direction, the positions of the inflow, lateral and outflow boundaries as well as several types of inflow and lateral boundary conditions. It has been found that the types of classically used inflow conditions tested (uniform or potential flow free-stream velocity) lead to an increase of the amplification rate (decrease of the critical Reynolds number) and Strouhal frequency which was practically independent of the type of condition used. The only way to eliminate this influence was to shift the inflow boundaries far enough upstream of the cylinder. The lateral free-stream condition results in a similar enhancement of the instability easily explainable by the amplifying effect due to an increased shear.

For the present mesh, the relatively small domain extension was estimated to be responsible for a less than 5% downward shift of the critical Reynolds number and for a 10% upward shift of the Strouhal frequency. The outflow boundary condition was found to cause an opposite trend, but for domains extending at least about 10 diameters downstream of the cylinder this effect appeared to be negligible (practically no reduction of the Strouhal number and a less than 1% increase of the critical Reynolds number). No spurious secondary frequencies resulting from boundary conditions such as those appearing in some compressible simulations (Abarbanel *et al.* 1991) were detected.

The increase of the number of collocation points results, in general, in a dampening of the instability. This can be explained by the numerical gradients of the flow field due to discontinuities at element interfaces. The discontinuities are the stronger the smaller the number of collocation points. The numerical gradients, then, tend to increase the shear effects in the near wake and destabilize the flow. This trend need not be completely monotonic but it has always been found to dominate. The fact that only 6 collocation points per element and space direction have been used was estimated to increase the Strouhal frequency by another 10% and decrease the critical Reynolds number by another 5% for the circular cylinder. A similar trend was found in the NACA wing configuration with a slightly non-monotonic convergence depending on the number of collocation points. The simulation of the onset of the Bénard–von Kármán instability in the two-dimensional domain obtained as a projection of the presented three-dimensional configuration could be compared to accurate results of Dušek *et al.* (1994*b*). A critical Reynolds number of about 43 and a critical Strouhal number of 0.14 have been found, the exact values being about 46 and 0.12, respectively. A similar overestimation of the Strouhal number appears in the two-dimensional simulations of Karniadakis & Triantafyllou 1989 (see also the comparison to experimental results in Williamson 1989) where an analogous mesh with a higher number of collocation points but with a less-optimized spectral element distribution was used.

It is more difficult to estimate the accuracy of the computation as far as purely three-dimensional effects are concerned. The latter have been found to be characterized by a low-frequency modulation of the wake oscillations. As a result the critical Reynolds number and the frequency of the modulation have to be computed for various meshes for this purpose. It is clear that the boundary plane situated as close as less than 4 cylinder diameters from the cylinder tip in the spanwise direction cuts off the secondary instability and is expected to have a dampening effect on the instability. There is, however, no blockage effect because a free-stream velocity condition is used and the dampening is not very strong. The influence of the spanwise confinement was tested on a mesh having an additional spectral element layer between $8 < z < 10$, i.e. extended in such a way that the distance between the cylinder tip and the spanwise boundary was increased to 7.1 diameters. The total number of spectral elements of this mesh was 142. In agreement with expectations, the primary oscillations, which are, basically, a two-dimensional effect, remained practically unaffected by this domain extension. In contrast, the beatings were stronger and had a higher frequency in the extended domain, the difference being, however, relatively moderate: about a 5% increase of the amplitude and about a 10% increase of the frequency.

The influence of the number of collocation points per element and space direction was tested by increasing their number from 6 to 8. Such a seemingly small increase of the discretization accuracy multiplies the computing costs by about a factor of 4. In agreement with expectations, the beatings have been found to have a significantly smaller amplitude which means that the critical Reynolds number of their onset (see §4) had been shifted upward. The level of the primary oscillations remained approximately the same and the basic (Strouhal) frequency even increased by about 3% which contradicted the trends obtained on two-dimensional meshes. Similarly, the frequency of the beatings increased. Undoubtedly the three-dimensional effects play a perceptible role in the capturing of the primary instability characteristics and a more systematic investigation of the three-dimensional discretization would be necessary to reveal the correct trends and their causes. Fortunately, the effects of these not fully understood trends are negligible with respect to dominating numerical errors.

The accuracy of the Navier–Stokes solution may also be influenced by the convergence of the pressure solver. To avoid this problem we adopted the strategy of setting the tolerance of the internal Poisson and Helmholtz inversion to a rather low level. It appears that the computing costs are not significantly increased and the zero divergence of the flow field is guaranteed. For the simulations performed, the average level of divergence varied between 10^{-4} and 2×10^{-4}. It must not be forgotten that the spectral element space discretization yields discontinuities of the derivatives at the element interfaces (Patera 1984) so that local values of divergence at element interfaces may be much higher than the average but the instability characteristics are determined by the average values.

A more detailed numerical investigation giving accurate bounds of the numerical errors of various relevant physical characteristics investigated by the simulation is possible but appeared to be prohibitively time consuming. Except for the small details mentioned above, the effects of the discretization inaccuracy could be roughly estimated and the errors brought under control. As a result, we do not expect that more accurate (and significantly more expensive) simulations would yield qualitatively different and quantitatively unexpected results. The chosen mesh represents a reasonable compromise allowing realistic simulations at acceptable costs with standard numerical techniques and computing equipment.

2.4. *'History' point distribution*

On-line monitoring of the simulation and rapid comparison to experimental hot-wire results was made possible by registering the velocity at 16 'history' points distributed throughout the computational domain. Their coordinates are assembled in table 1 and the numbering will be, from time to time, referred to in the text. 31 history points distributed symmetrically with respect to the symmetry plane $z = 0$ were used in the full cylinder configuration. In the NACA wing mesh similarly distributed history points were also used.

Point	x	y	z	Point	x	y	z
1	1.591	−0.4688	3.213	9	3.515	−0.2859	0
2	1.591	−0.4688	5.883	10	7.280	−0.2859	5.643
3	1.591	0	3.213	11	7.280	0	5.643
4	1.591	0	5.883	12	7.280	−0.8000	5.643
5	3.515	−0.2859	3.213	13	7.280	0.0939	3.213
6	3.515	−0.2859	5.883	14	7.280	0	3.213
7	3.515	0	5.883	15	7.280	−0.2859	3.213
8	3.515	0	3.213	16	7.280	−0.5141	3.213

Table 1. Coordinates of 'history' points of the simulation of flow past the half-cylinder of aspect ratio $L/d = 21.4$ in units such that $d = 0.56$

3. Primary (Bénard–von Kármán) instability in three dimensions

The primary instability in the wake of finite cylinders is a phenomenon that has been described many times experimentally and numerically. It is well known that, in the central symmetry plane, the instability is, except for small effects due to the finite aspect ratio investigated by Mathis (1983) and more recently by Albarède & Provansal (1995), practically identical with that obtained in a perfectly two-dimensional case. The spatial envelopes along the flow axis have been measured experimentally by Mathis (1983). Recently Goujon-Durand, Jenffer & Wesfreid 1994 examined the deformation of these envelopes with increasing Reynolds number. The full spatial description of the instability limit cycle has been obtained from a numerical simulation in Dušek (1996). Present experimental techniques make it possible to also measure the envelopes of the lowest instability harmonics fully in two dimensions using laser Doppler anemometry (Wesfreid, Goujon-Durand & Zielinska 1996) or Ultrasound Velocimetry (Peschard 1995). As far as the strongly three-dimensional aspects of the primary instability near the ends of the finite cylinders are concerned, the paper of Gerich & Eckelmann 1982 mentions the existence of a narrow interval of Reynolds numbers where only one frequency can be found in the flow. The amplitudes of oscillations with this frequency have been found to vanish close to the cylinder ends. As will be shown in this study, this interval is the shorter the greater the aspect ratio so that for large aspect ratios such as those referred to in König *et al.* (1990, 1992, 1993) or Brede *et al.* (1994), it may be difficult to detect.

3.1. *Limit cycle characterization*

Before presenting the three-dimensional structure of the primary instability let us discuss its character. In Dušek *et al.* (1994*b*), it has been shown that the two-dimensional Bénard–von Kármán instability reaches a strict limit cycle. It is easy to carry out two-dimensional simulations at unphysically high Reynolds numbers (> 200) to show that this limit cycle remains stable as long as the transition to three-dimensionality is inhibited. The observed presence of two or several incommensurate frequencies in three-dimensional wakes at very low Reynolds numbers proves that the limit cycle of the primary instability is often not very stable and the question may arise whether a, strictly speaking, stable limit cycle exists at all in three dimensions. Recall that Benjamin & Feir (1967) showed that waves on deep water, which can be considered as a primary instability at the water surface, are always unstable, i.e. can never reach a perfect limit cycle. A simple way to check the existence of the limit cycle is to investigate the period of the simulated velocity signal in various zones of the flow over a long time.

As has already been mentioned in the previous section, the instability develops spontaneously at Reynolds numbers exceeding $Re_1 = 43$ with our space and time discretization accuracy. At slightly supercritical Reynolds numbers $Re = 45, 47$ and 49, we let the instability reach saturation and measured the simulated frequency of the oscillations at all 16 history points. Note that only one point had been placed in the symmetry plane where the behaviour was expected to be very nearly two-dimensional and that, on the contrary, most of the history points had been distributed at various distances downstream of the zone close to the cylinder tip where a more complex behaviour was always experimentally observed. At all points and for all velocity components, we also plotted the three values of the square of the amplitude so obtained and found a very nearly linear trend, from which we estimated the critical Reynolds number value given above.

Analogous simulations have been carried out for the NACA wing at Reynolds number values based on the inflow velocity and the wing chord of $Re = 76$, 77 and 80. The critical Reynolds number, based on the profile chord c, was found to be $Re_1 = 74$. If, instead, a Reynolds number Re' based on the effective cross-section width $c\ \sin(\alpha)$, with α the incidence angle, is used this critical value corresponds to $Re' = 41$, which is practically the same as for the circular profile.

At each point, the period T was determined on the basis of the simulated velocity signal for all the three velocity components by taking twice the mean time corresponding to crossing the mean value and an average was taken over the three components. The Strouhal number values so computed at all history points have been found uniform with an accuracy of about 1 to 2 per thousand. The Strouhal number varies only very slowly as a function of the Reynolds number. By extrapolating the slightly supercritical Strouhal number values to the critical Reynolds number we find a critical Strouhal number of $St_1 \approx 0.143$. All these simple results can be summed up as a confirmation of the well-known fact that the primary instability arises as a result of a supercritical Hopf bifurcation. Close to the critical Reynolds number for the onset of oscillations the flow reaches a stable limit cycle with an oscillation period which is uniform in space.

The limit cycle can be best characterized by its harmonics. In Dušek *et al.* (1994*b*) a temporal Fourier decomposition of the Navier–Stokes equations was proposed. It is based on a separation of the periodic behaviour, expanded in a Fourier series, and of the non-periodic transients, accommodated by time-dependent Fourier coefficients. The method appeared to be not only of theoretical interest but also provided a basis for an efficient numerical algorithm applicable to the investigation of instabilities (Carte *et al.* 1995). The pressure–velocity formulation of the Fourier decomposition of the Navier–Stokes equations is also described in Carte *et al.* (1995).

At saturation (i.e. when the limit cycle is reached) the velocity and pressure fields become strictly periodic and the expansions described in Carte *et al.* (1995) become genuine Fourier expansions with time-independent coefficients:

$$\boldsymbol{v}(t,.) = \sum_{n=-\infty}^{+\infty} \boldsymbol{c}_n^{(1)}(.)\, \mathrm{e}^{in\omega^{(1)}t} \tag{1}$$

and

$$p(t,.) = \sum_{n=-\infty}^{+\infty} d_n^{(1)}(.)\, \mathrm{e}^{in\omega^{(1)}t}. \tag{2}$$

The superscript $^{(1)}$ in (1) and (2) refers to the limit cycle of the primary instability.

The Fourier coefficients $\boldsymbol{c}_n^{(1)}$ and $d_n^{(1)}$ are, respectively, vectorial and scalar complex functions in space; the angular frequency $\omega^{(1)}$ is that of the saturated instability. The velocity and pressure being real, we have

$$\overline{\boldsymbol{c}_n^{(1)}} = \boldsymbol{c}_{-n}^{(1)}, \quad \overline{d_n^{(1)}} = d_{-n}^{(1)}. \tag{3}$$

The Fourier coefficients $\boldsymbol{c}_n^{(1)}$ and $d_n^{(1)}$ satisfy the following system of coupled equations:

$$\left(in\omega_1 - \frac{1}{Re}\nabla^2\right)\boldsymbol{c}_n^{(1)} + \sum_{k=-\infty}^{+\infty}\left(\boldsymbol{c}_k^{(1)}\cdot\nabla\right)\cdot\boldsymbol{c}_{n-k}^{(1)} + \nabla d_n^{(1)} = 0, \tag{4}$$

$$\nabla\cdot\boldsymbol{c}_n^{(1)} = 0. \tag{5}$$

yielding a time-independent limit cycle description.

The advantage of the characterization of the limit cycle by its Fourier coefficients is that it reduces the cycle to a fixed point in a more complex space. This space is actually not much more complex that the original unsteady velocity–pressure representation because only a limited number of harmonics characterize accurately the flow near the primary instability threshold (see Carte *et al.* 1995, 1996 and Dušek 1996). To obtain a quite accurate description of the limit cycle of the instability a small number of complex steady space functions replace the four unsteady real functions which are the velocity vector and the pressure.

3.2. *Computation of Fourier components*

In this paper, we do not investigate the transient process of convergence to the limit cycle: we focus directly on the flow after the limit cycle has been reached. The expansion (1) of the velocity field is computed from a direct solution of unsteady Navier–Stokes equations. The harmonics of the flow field have been computed throughout the whole domain by integrating the Fourier coefficients over one period of the flow oscillation. It has been done by the on-line post-processing described in Dušek (1996) to avoid storing the intermediate instantaneous flow fields. The on-line integration over one period allows any number of harmonics to be computed and limits the additional storage capacity required only to the complex fields of the considered Fourier components. Its advantage in comparison to fitting the Fourier expansion to a limited number of selected flow field dumps is that it averages over all intermediate values and reduces numerical errors. The integration period was determined automatically at point 9 of table 1. For the cylinder, this point lies in the symmetry plane close to the flow axis ($y = 0, z = 0$). On the flow axis the oscillations of the v-velocity are maximal and the mean value is identically zero because of the symmetry of the configuration. The selected point lying slightly off the symmetry plane $y = 0$, the mean value of the v-velocity is not exactly zero there. The period was thus obtained simply by registering every second zero crossing of the transverse (v-) velocity signal at this point. The computing costs of the integration are negligible if only a small number of harmonics are taken into account. We limited ourselves to computing only the mean value, the first and the second harmonics. It appeared that practically all information about the flow field was represented by these three lowest Fourier components at the low Reynolds numbers considered, the higher harmonics representing a correction of the order of 1%.

We present the results only for the cylinder wake at $Re = 49$ obtained in the half-configuration. The primary instability breaks the symmetry with respect to the plane defined by the cylinder axis and the inflow velocity direction but it is not expected to

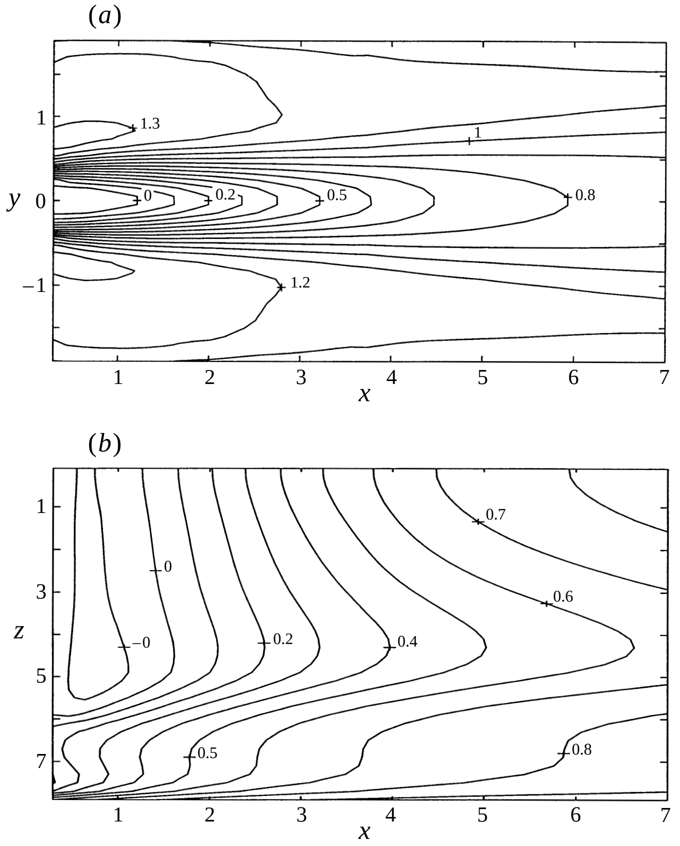

FIGURE 2. Iso-velocity plot of the u-velocity mean value downstream of the cylinder in the symmetry plane $z = 0$ (*a*) and in the $y = 0$ plane containing the cylinder axis (*b*). The cylinder extends to $z = 6$. Note the strong velocity deficit near the cylinder end. ($Re = 49$, $L/d = 21.4$.)

break the symmetry with respect to the symmetry plane normal to the cylinder. Indeed, a simulation with a slightly asymmetrical initial condition in the full configuration at $Re = 49$ confirmed this expectation. As a result, the simulations in the half-domain can be considered as an exact representation of the full domain flow. Symmetry breaking does not mean that the symmetry gets totally lost (Crawford & Knobloch 1991). Although the instantaneous flow has no longer the symmetry properties of the steady flow, the mean flow and the harmonics do still keep well-defined symmetry properties (Dušek 1996). The flow past the asymmetrically positioned wing is very similar except that symmetry properties hold only asymptotically.

3.3. *Mean value*

Figure 2 shows the mean value $c^{(1)}_{u,0}$ of the streamwise (u-) velocity downstream of the cylinder in the $z = 0$ symmetry plane and in the plane containing the cylinder axis ($y = 0$). Figure 2(*a*) ($z = 0$-plane) is indistinguishable from that obtained in a two-dimensional simulation. The three-dimensional effects are visible in figure 2(*b*). Recall that the length units are such that the cylinder diameter is 0.56 and it extends from $z = 0$ (the symmetry plane) to $z = 6$. Note that there is actually a minimum of the velocity deficit on the flow axis ($y = 0, z = 0$), the maximum lying between $z = 4$ and $z = 5$, i.e. only about 3 cylinder diameters from the cylinder end. The origin

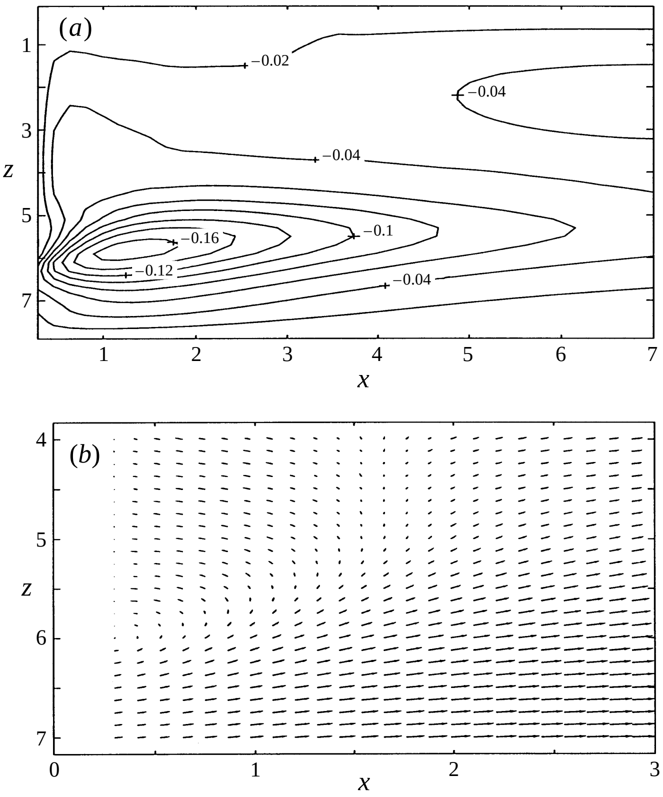

FIGURE 3. Iso-velocity plot of the spanwise (w)-velocity mean value (a) and (u, w) velocity vector plot (b) downstream of the cylinder in the plane containing the cylinder axis ($y = 0$) showing the strong recirculation past the cylinder end. ($Re = 49$, $L/d = 21.4$.)

of this maximum of the velocity deficit can easily be explained by the recirculation around the cylinder end. Indeed, the strong vortex of the mean velocity field ($\boldsymbol{c}_0^{(1)}$) downstream of the cylinder end is clearly visible in figure 3.

3.4. *Fundamental harmonic*

Regarding the fundamental harmonic $\boldsymbol{c}_1^{(1)}$ of the instability, figure 4 represents the known (Goujon-Durand *et al.* 1994; Wesfreid *et al.* 1996; Dušek 1996) typical two-dimensional structure of the fundamental of the transverse velocity $c_{v,1}^{(1)}$. The wavy character of the crest of the envelope of the fundamental represented in the figure 4(a) is due to the presence of the spectral element interfaces and to the insufficient spatial resolution. 12% above the instability threshold the experimental data and numerical two-dimensional simulations lead to the maximum of the mode being expected at about 7 diameters (at $x \approx 4$) downstream of the cylinder. The iso-phase plot (figure 4b) is obtained by plotting iso-lines of $\cos(\varphi)$, φ being the phase of the complex function $c_{v,1}^{(1)}$ at levels $\pm\sqrt{2}/2$, representing phases $\pm\pi/4$ and $\pm\pi/4+\pi$. A double line (obtained by plotting two levels of cosine very close to $\sqrt{2}/2$) is used to distinguish the values $\pm\pi/4$ from $\pm\pi/4 + \pi$. The phase plot shows the transverse deformation of the propagating wave of the fundamental and allows the wavelength near the outflow of the domain to be estimated as 6.1 cylinder diameters which agrees again with two-dimensional simulations and experimental results of

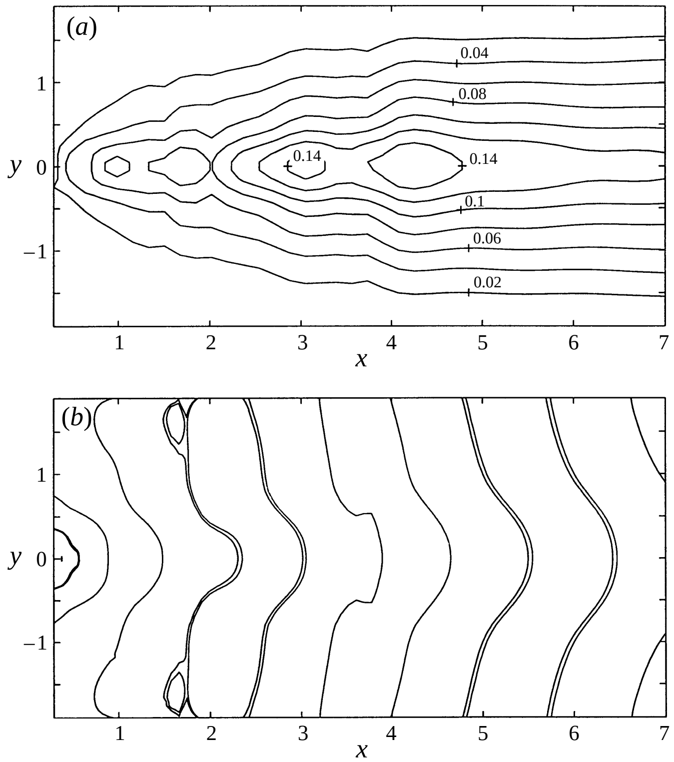

FIGURE 4. Representation of the fundamental of the v-velocity in the symmetry plane $z = 0$: (*a*) iso-amplitude plot, (*b*) iso-phase plot. The iso-phase plot is obtained by plotting $\cos(\varphi)$, φ being the phase. The double line represents the $\varphi = \pm\pi/4$, the single one $\varphi = \pm\pi/4 + \pi$. ($Re = 49$, $L/d = 21.4$).

Williamson for the same value of the instability parameter $(Re - Re_1)/Re_1$. It is interesting to see how the fundamental changes in the spanwise direction. If the transverse structure is plotted in various $z =$ *const.* sections it can be seen that the form of the envelope as well as the phase plots are almost the same except that the amplitude decreases as the cylinder ends are approached. Figure 5 shows the envelope of the fundamental in the plane containing the cylinder end. The envelope is only a little more elongated, but the maximum lies always approximately 7 diameters downstream of the cylinder. The amplitude is about 35 times smaller than in the symmetry plane $z = 0$. Off the symmetry plane, the spanwise (w-) velocity component is non-zero. The symmetry properties with respect to the $y = 0$ plane of the w-velocity component are the same as those of the streamwise (u-) velocity (see Dušek *et al.* 1994*b*). As a result, the fundamental $c^{(1)}_{w,1}$ is antisymmetric with respect to the $y = 0$ plane, i.e. its envelope has two lobes, each corresponding to opposite phases of oscillations.

To show the spanwise structure of the fundamental we visualized its envelope and phase in the plane $y = 0$ containing the cylinder axis. In figure 6(*a*), the envelope of the v-velocity is plotted in the form of iso-lines of its logarithm $\log_{10}(|c^{(1)}_{v,1}|)$ to make its progressive decrease past the cylinder end more visible. The iso-phase plot of $c^{(1)}_{v,1}$ in figure 6(*b*) is representative of the spanwise form of the vortices in the wake. The

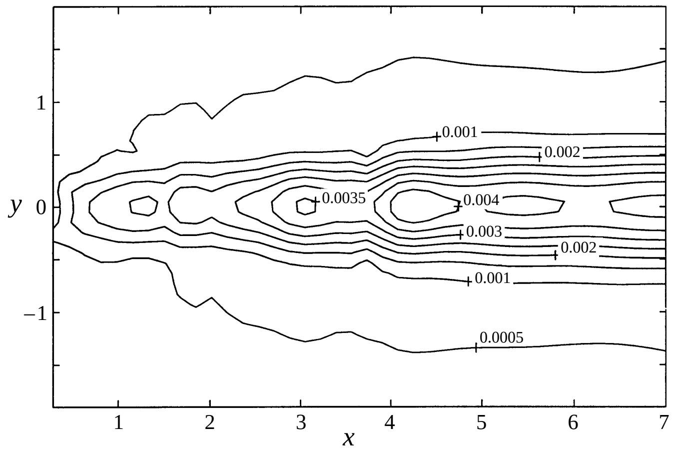

FIGURE 5. Iso-amplitude plot of the fundamental of the v-velocity in the plane containing the cylinder end $z = 6$. ($Re = 49$, $L/d = 21.4$.)

similarity with the ‘low speed mode’ visualization of Tritton (1959) is obvious. The structure of envelopes of the individual components of the fundamental harmonic is determined by their symmetry properties. The v-velocity fundamental is symmetric with respect to both the $y = 0$ and the $z = 0$ planes so that its envelope has only one lobe as seen in figures 4 and 6. The u-velocity fundamental is symmetric with respect to the $z = 0$ plane but antisymmetric with respect to the $y = 0$ plane so two lobes of the envelope exist and are separated by the $y = 0$ plane as can be seen in two-dimensional visualizations (Dušek 1996). The w-velocity fundamental $c_{w,1}^{(1)}$ is antisymmetric with respect to both the $y = 0$ and $z = 0$ planes, which implies that it is identically zero in these planes and its envelope has four lobes.

3.5. *Higher harmonics*

In Dušek *et al.* (1994*b*) the symmetry properties of all the harmonics of the two-dimensional cylinder wake have been specified by giving the symmetry properties of the stream-function Fourier components. The Fourier components of the velocity vector field are discussed in two dimensions in Dušek (1996). In three dimensions, the geometry possesses two symmetry planes $y = 0$ and $z = 0$ for the finite circular cylinder. The broken symmetry with respect to the $y = 0$ plane yields the more complex symmetry properties for the u- and v-velocity harmonics and for the scalar functions presented already in the two-dimensional case. The symmetry of the w-velocity harmonics with respect to this symmetry plane is the same as for the u-velocity. The symmetry properties with respect to the $y = 0$ plane can be summarized up as follows:

$$\left.\begin{aligned} d_n(x,-y,z) &= (-1)^n d_n(x,y,z),\\ c_{u,n}(x,-y,z) &= (-1)^n c_{u,n}(x,y,z),\\ c_{v,n}(x,-y,z) &= (-1)^{n+1} c_{v,n}(x,y,z),\\ c_{w,n}(x,-y,z) &= (-1)^n c_{w,n}(x,y,z). \end{aligned}\right\} \qquad (6)$$

In (6) we dropped the superscript $^{(1)}$ because they hold also for the transients if they are satisfied by the initial condition. In contrast, the symmetry with respect to the $z = 0$ plane is not broken and the ordinary scalar and vector symmetry representation

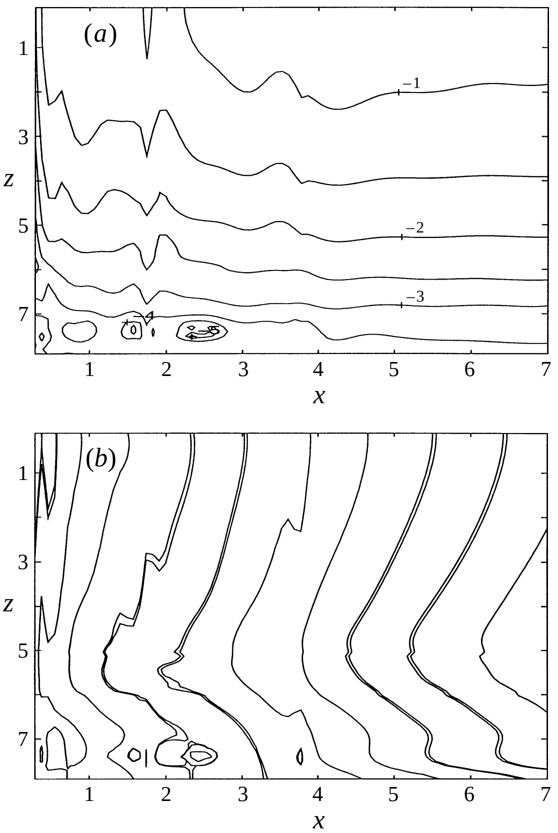

FIGURE 6. Cross-section of the v-velocity fundamental in the plane containing the cylinder axis $y = 0$. (a) Iso-lines of the common logarithm of the envelope. (b) Iso-phase plot (see caption of figure 4). ($Re = 49$, $L/d = 21.4$.)

holds for all harmonics:

$$\left.\begin{aligned} d_n(x,y,-z) &= d_n(x,y,z), \\ c_{u,n}(x,y,-z) &= c_{u,n}(x,y,z), \\ c_{v,n}(x,y,-z) &= c_{v,n}(x,y,z), \\ c_{w,n}(x,y,-z) &= -c_{w,n}(x,y,z). \end{aligned}\right\} \tag{7}$$

As a consequence, the three-dimensional case does not add anything fundamentally new in comparison with the two-dimensional one. The transverse structure of the higher harmonics of the v- and u-velocity has been found qualitatively the same as in two dimensions (see Dušek 1966), while for the w-velocity component, its symmetry properties (6) suggest, and visualizations confirm, that the transverse structure of its harmonics is much the same as for the u-velocity component. The spanwise structure is simple for all harmonics and influenced by the symmetry properties (7), i.e. the u- and v-velocity harmonics have their maxima in the $z = 0$ plane like the v-velocity fundamental plotted in figure 6. The maximum of the w-velocity harmonics lies off this plane because of the antisymmetry of the w-velocity with respect to the $z = 0$ plane.

The wake of an asymmetric object such as that of the NACA wing with incidence considered keeps many of the properties resulting from the symmetry relations (6) in spite of the fact that there is no longer a strict symmetry with respect to the $y = 0$ plane. This can be explained by the fact that the asymmetry is really felt only in the near wake but that, asymptotically, the shape of the object plays only a limited role. Similarly, the symmetry of the far wake with respect to the $z = 0$ plane remains even if the obstacle is slightly tilted. In the far wake the symmetry properties (6), (7) are fully recovered even for non-symmetric obstacles. An asymmetric but elongated object thus generates a wake still possessing two asymptotic symmetry planes.

4. Secondary instability

4.1. *Onset of modulation of wake oscillations*

When the Reynolds number is increased we observe the onset of modulation of the wake oscillations similar to that reported in experiments (Tritton 1959; Gaster 1969, 1971; Gerich & Eckelmann 1982; König *et al.* 1990). At $Re = 54$ the modulation is clearly present whereas a simulation starting with an initial condition corresponding to the flow with modulation at $Re = 54$ but run at $Re = 52$ shows the modulation amplitude vanishing exponentially (figure 7). Figure 7 shows signals of transverse (v-) velocity at the same point (point 8) in the $y = 0$ plane about 6 diameters downstream of the cylinder and about half-way between the symmetry plane ($z = 0$) and the cylinder end, but the same behaviour can be observed everywhere, in particular also in the symmetry plane (point 9). The modulation is thus clearly a global phenomenon and its threshold of onset lies at $Re_2 \approx 53$ (for the numerical discretization used). Gaster (1969) notes that the beatings in the wake of a slender cone are noteworthy for their uniform frequency throughout the flow in spite of the fact that rapid oscillations within the beatings are found to vary spanwise and to obey the Roshko law based on the local Reynolds number of the cone. Gerich & Eckelmann (1982) find that the frequency of modulation (beatings) corresponds exactly to the difference of the wake frequencies found in the ‘affected’ and ‘unaffected’ regions of the wake and that in both regions the basic frequency is uniform. This means that they, too, observe the same frequency of modulation whether they measure the velocity fluctuations in the central zone of the cylinder or near its tips. The first point is thus to see whether the modulation in our simulation is, indeed, uniform throughout the flow in the same way as it was the case for the frequency of the primary instability.

4.2. *Hopf-like character of the secondary bifurcation*

For this purpose the period of the modulation was calculated at all the 16 history points of table 1 at $Re = 54$. The non-dimensionalized value of the modulation frequency was found to be $St^{(2)} = 0.00876 \pm 0.00001$ at all history points. The uniformity of the period of the modulation has thus been clearly confirmed. Similar simulations with a sufficiently long run to reach a steady modulation amplitude were carried out at $Re = 58$ and $Re = 62$. At $Re = 100$ the attractor was not perfectly reached but the simulation at this Reynolds number gives a good indication of the trend at higher Reynolds number values. In all cases the uniformity of the modulation frequency in space has been confirmed. The dependence of the square of the local beating amplitude on the three nearly critical Reynolds number values considered (54, 58, and 62) at a point situated in the $z = 0$ plane and the respective Strouhal *vs.* Reynolds number dependence are plotted in figure 8. The Strouhal number is the simulated frequency of modulation non-dimensionalized by the inflow velocity of 1 and the cylinder diameter of 0.56. (The deviation from nonlinearity in figure 8 is due to the fact that the Reynolds number interval [54,62] is not quite small. The

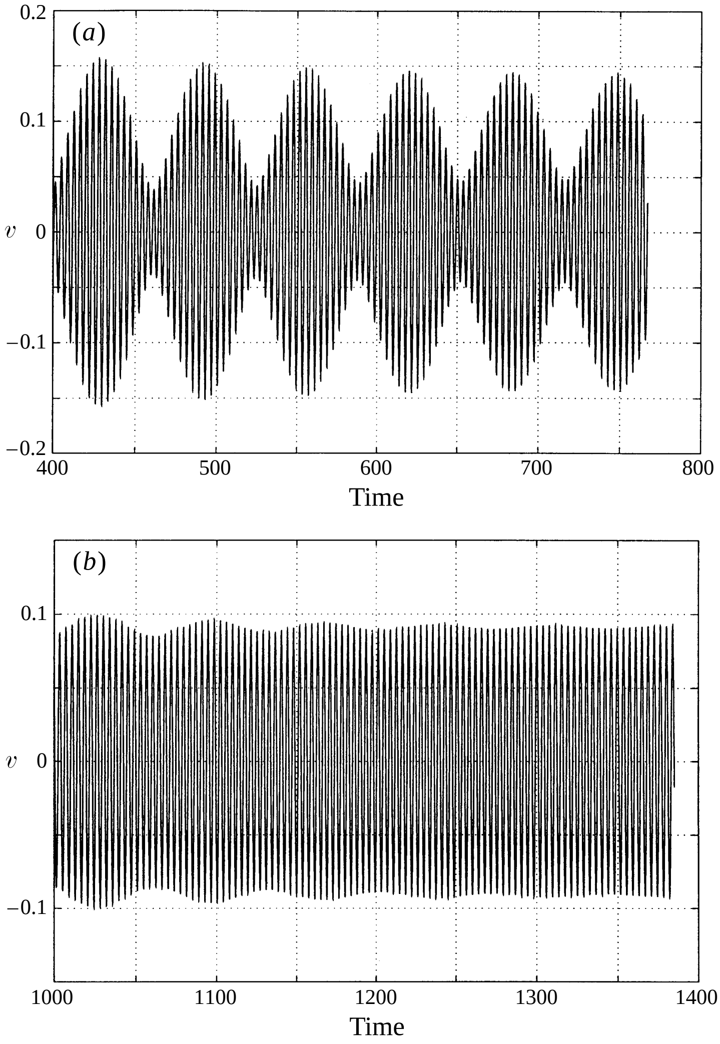

FIGURE 7. Onset of the secondary instability at $Re \approx 53$. (a) Modulation of the v-velocity oscillations at $Re = 54$ at the point $x = 3.5, y = 0, z = 3.2$. (b) Decay of the modulation observed at the same point as above in a run at $Re = 52$. ($L/d = 21.4$.)

Roshko *vs.* Reynolds number dependence approaches linearity much better.) An extrapolation of the graphs in figure 8 shows that the critical Reynolds number of the onset of the beatings lies clearly above the threshold of the primary instability. We find $Re_2 = 53.5$ which is about 24% above $Re_1 = 43$. The critical Strouhal number is about 0.0086 with a very slow increasing trend $\mathrm{d}St/\mathrm{d}Re \approx 2.6 \times 10^{-4}$ leaving no doubt that this value is non-zero. Three values in figure 8 may seem inadequate to draw a curve through. It should, however, be pointed out that the three values plotted are essentially accurate within the dynamical model represented by the chosen space-time discretization. The ultimate confirmation of the fact that the threshold lies between $Re = 52$ and $Re = 54$ and that the critical Strouhal number is non-zero is given in figure 7. We can thus conclude that the secondary bifurcation is again of Hopf type.

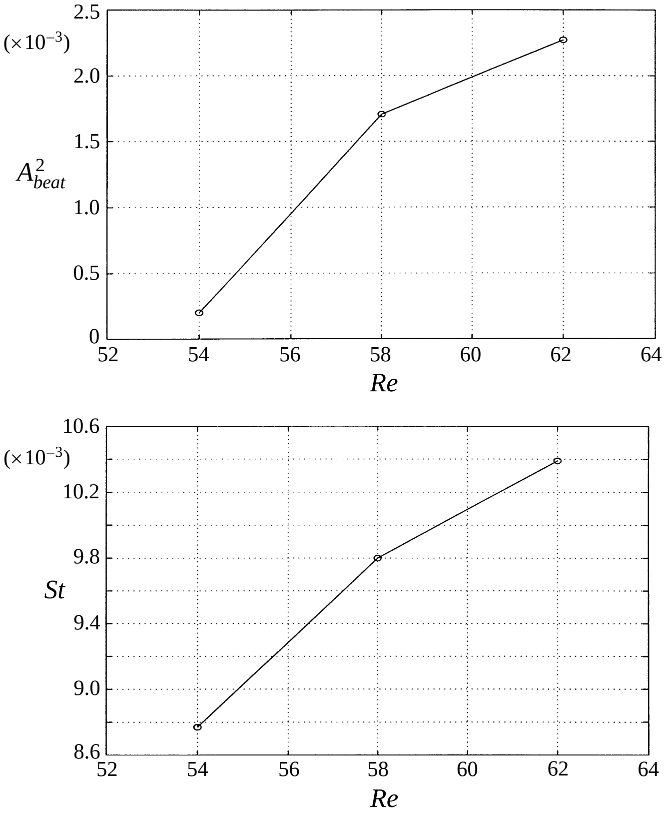

FIGURE 8. (*a*) Square of the modulation amplitude *vs.* the Reynolds number. (*b*) Strouhal number of the modulation *vs.* the Reynolds number. Values obtained by processing the simulated signal at $x = 3.5, y = -0.286, z = 0$. ($L/d = 21.4$.)

4.3. *Symmetry with respect to the* $z = 0$ *plane*

Before analysing the new instability in more detail we have to answer the question whether the half-domain with the symmetry boundary condition in the $z = 0$ plane used to simulate the whole configuration is still adequate. For this purpose we ran a simulation in the full domain on a mesh obtained by adding the mirror image of the half-domain on the other side of the symmetry plane. The simulation was carried out for both aspect ratios $L/d = 21.4$ and $L/d = 10.7$. The initial condition for $L/d = 21.4$ was constructed from the final state of the simulation at $Re = 54$ in the half-domain by taking the symmetric flow with respect to the $z = 0$ plane. The easiest way how to recognize symmetry breaking is to monitor the spanwise w-velocity in the symmetry plane. A slight perturbation of the symmetry appeared. The w-velocity oscillations had, however, a very low level of 10^{-5} representing about 0.1% of the overall maximum of their amplitude (about 0.02 at $x/d = 7$, $y/d = \pm 1$ and $z = \pm 5$) and had a very slow, but existent, trend to decrease. The same result was found by comparing the other velocity components (u and v) at points situated symmetrically with respect to the symmetry plane. The asymmetry was found not to exceed 0.4% of the velocity oscillation amplitude. For the smaller aspect ratio of $L/d = 10.7$, symmetry conservation was also confirmed. For this configuration, the simulation was performed at $Re = 100$ and started from a perfectly symmetric flow obtained at a lower Reynolds number (80). The start of the run was thus characterized by a Reynolds number jump. This appeared to be sufficient to trigger spanwise (w-) velocity oscillations in the $z = 0$ symmetry plane of about a 10^{-3} amplitude but these oscillations finished by decaying after about 100 primary Strouhal periods to the 10^{-5} level. The initial symmetry perturbation for $L/d = 21.4$ and $Re = 54$ is thus explained as a result of a not perfectly established flow taken as initial condition. The stability of the symmetry appears to be very weak but to exist.

Though no symmetry breaking was found at the secondary instability onset for the aspect ratios considered, symmetry breaking might be expected at higher Reynolds number or smaller aspect ratio. Jayaweera & Mason (1965) report a flutter of falling cylinders significant only for cylinders with an aspect ratio L/d below a certain value. In the limit case of a very flat cylinder, antisymmetric von Kármán vortex shedding in the $z = 0$ plane occurs. The phenomenon might be similar to that of interacting wakes (see Le Gal *et al.* 1990) with symmetry for long cylinders and antisymmetry for short ones. The secondary instability described in this paper might not be relevant for this symmetry transition because it tends to disappear for small aspect ratios (see §7). A systematic investigation of what happens for small aspect ratios is thus a very interesting issue.

Finally we compared the velocities simulated in the full domain with those obtained in the half-domain to test if taking the full domain had a significant influence on the secondary instability development. We found that the difference was negligible and that it decayed in the same way as the asymmetry described above. We conclude that, at least for the relatively large aspect ratios considered, the symmetry with respect to the $z = 0$ plane is conserved and that the half-domain simulation accounts perfectly for the dynamics of the full length configuration.

5. Nature of the attractor

5.1. *Uniform or spatially variable primary frequency*

The signal of the transverse velocity at $Re = 54$ presented in figure 7(*a*) suggests that an attractor is reached. The uniformity of the modulation period allows the application of a global Fourier decomposition with this period. However, as pointed out in the introduction, some experimental results tend to indicate that the originally uniform primary frequency varies throughout the flow field. A way of calculation of the primary frequency consists of computing the ‘instantaneous period’ of the oscillations. The latter being no longer really periodic, this value is obtained as the time between two crossings of a given value in the same (upward or downward) direction. In figures 9, 10, 11 we present, respectively, the local v-velocity signal, its spectrum and its ‘instantaneous Strouhal number’ (in quotation marks because it is based on the ‘instantaneous period’ just defined) at $Re = 62$ at three points distributed spanwise about 6 diameters downstream of the cylinder. One point lies in the symmetry plane (part *a*, point 9 of table 1), the second lies halfway between the symmetry plane and the cylinder end in the spanwise direction (part *b*, point 8) and the third point lies downstream of the cylinder end (part *c*, point 7).

In figure 9 the modulation period is clearly the same at the three points and equal to 53.9 time units. The time obtained by dividing the cylinder diameter d by the inflow velocity is equal to 0.56 time units, i.e. the corresponding Strouhal number of the beating is $St^{(2)} = 0.0104$. In figure 10 we can detect the principal frequencies responsible for the beatings. In figure 10(*a*), we identify a principal

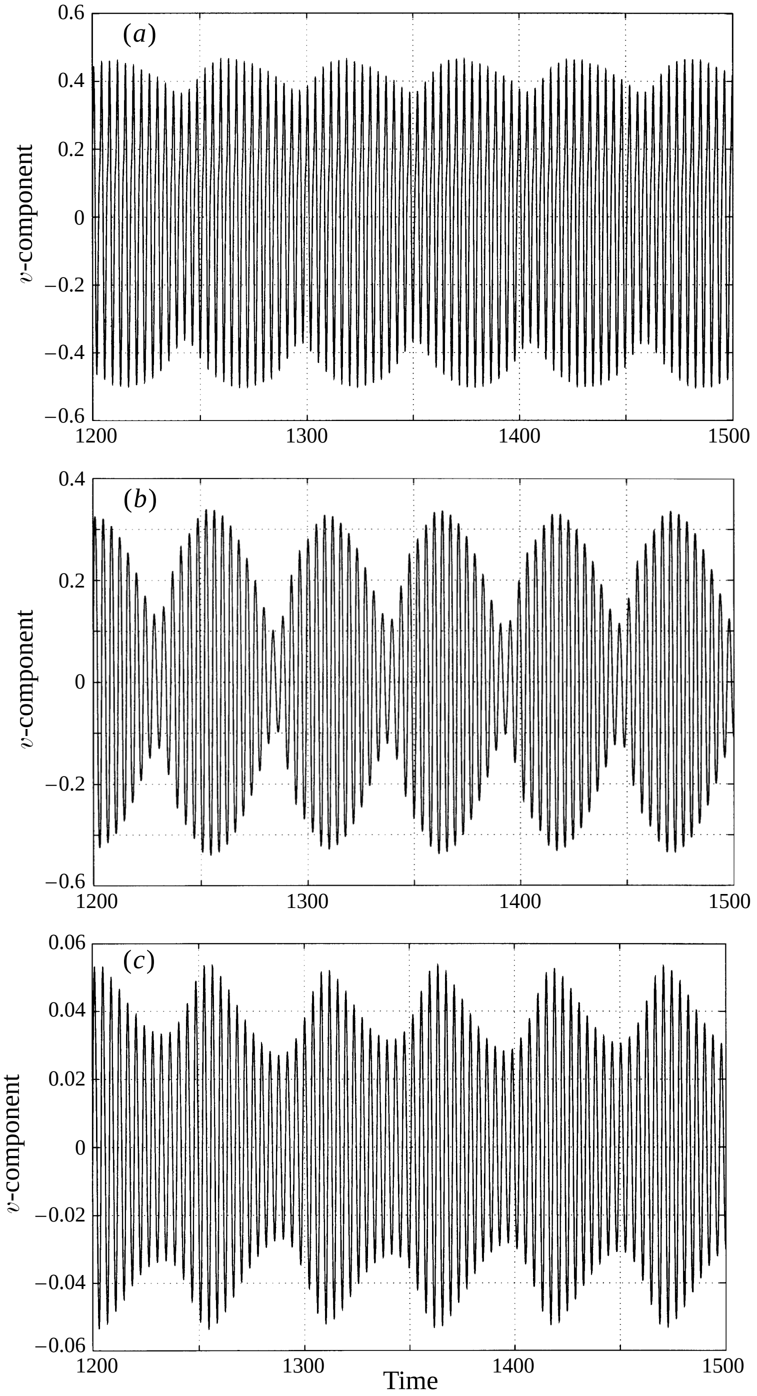

FIGURE 9. Simulated v-velocity signal at $Re = 62$ at (a) a point in the symmetry plane but slightly off the $y = 0$ plane ($x = 3.5, y = -0.3, z = 0$), (b) a point halfway between the symmetry plane and the cylinder end in the streamwise direction ($x = 3.5, y = 0, z = 3.2$) and (c) a point downstream of the cylinder end ($x = 3.5, y = 0, z = 5.9$), both last points lying in the $y = 0$ plane. ($L/d = 21.4$.)

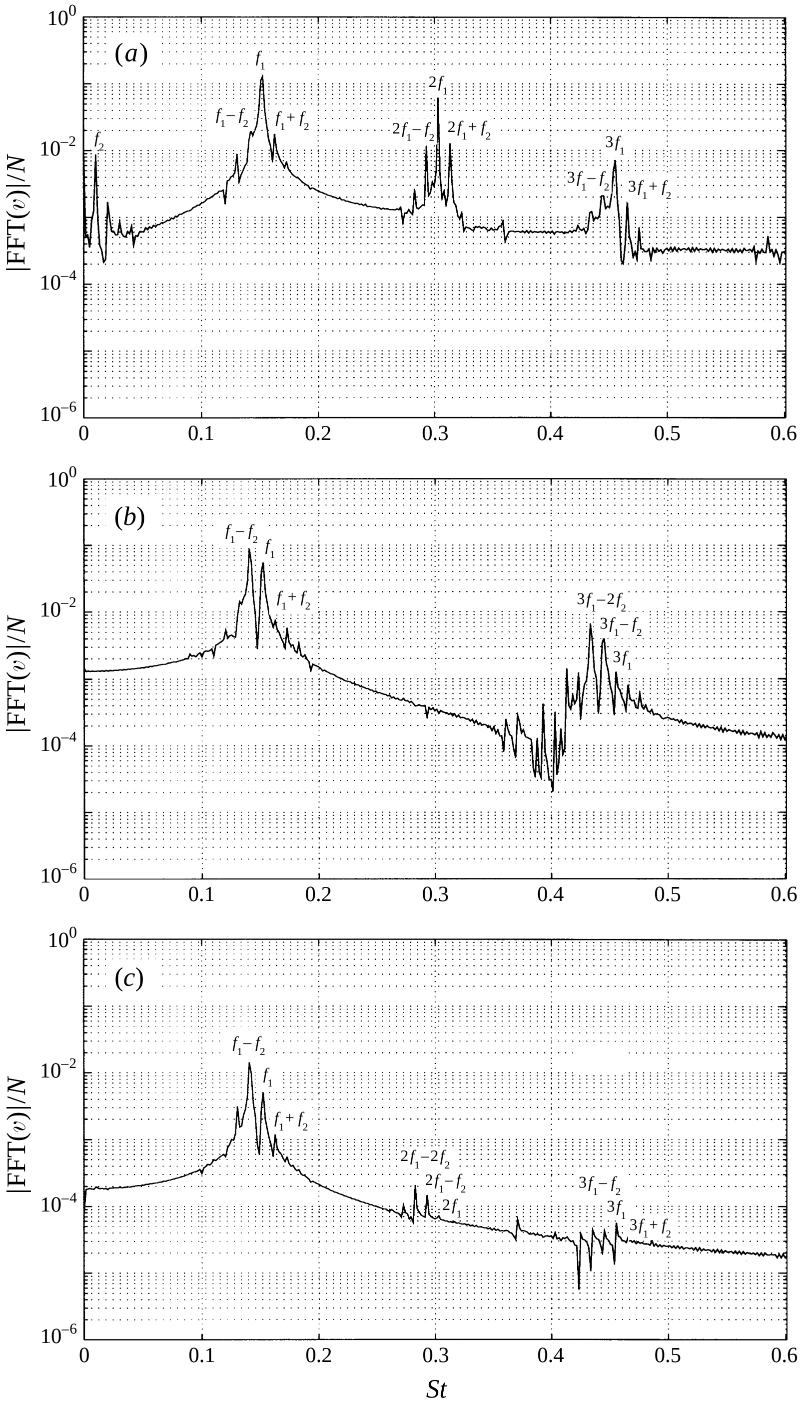

FIGURE 10. Spectra – absolute values of the Fourier transforms of the signals in figure 9. The symbols f_1 and f_2 stand for $St^{(1)}$ and $St^{(2)}$, respectively, and are used to mark the peaks corresponding to linear combinations of these frequencies.

Strouhal number $St_{sym} = 0.1520$ and two, about one order of magnitude smaller, lateral peaks corresponding to $St_{sym} \pm St^{(2)}$. (In order to obtain legible symbols f_1 stands for St_{sym} and f_2 for $St^{(2)}$ in the figure.) The corresponding point lying in the symmetry plane, we denote temporarily the non-dimensionalized frequency of the main peak St_{sym}. In figure 10(*b*), two frequencies of almost equal amplitude dominate. The slightly higher peak corresponds to $St_{sym} - St^{(2)}$ the other is that of St_{sym}. In figure 10(*c*) the situation is very similar to that of 10(*a*) except that the highest peak corresponds to $St_{sym} - St^{(2)}$ and the lateral (and significantly smaller) ones are $St_{sym} - 2St^{(2)}$ and St_{sym}. In figure 11 the 'instantaneous Strouhal numbers' of the primary oscillations are plotted twice per Strouhal period (open circles) and joined by a continuous line. The time scale being the same as in figure 9 it can easily be seen which values correspond to the maximum amplitudes of the beatings used to evaluate the local Strouhal number in Gaster (1969). It is clear that the frequency corresponding to the maximum amplitude varies strongly from one signal to another. Moreover, in part (*a*) (point in the symmetry plane) the frequency maxima correspond to the lowest amplitudes, whereas in part (*b*) (point half-way between the cylinder end and the symmetry plane) and part (*c*) (point downstream of the cylinder end) they correspond to the maximum amplitudes. This seemingly amazing behaviour can easily be explained.

Let us consider oscillations described by the real part of the following complex expression:

$$z(t) = \left[a_{1,0} + a_{1,1}\mathrm{e}^{\mathrm{i}\Omega t} + a_{1,-1}\mathrm{e}^{-\mathrm{i}\Omega t}\right]\mathrm{e}^{\mathrm{i}\omega t}. \tag{8}$$

In figure 12(*a*) we plot the curve described by the expression in the square brackets for arbitrarily chosen values: $a_{1,0} = \mathrm{e}^{\mathrm{i}\pi/3}$, $a_{1,1} = 0.2\mathrm{e}^{\mathrm{i}\pi/6}$, $a_{1,-1} = 0.1\mathrm{e}^{-\mathrm{i}\pi/3}$, $\omega = 2\pi$ and $\Omega = 0.2\pi$. It is an ellipse circumscribed with a period $2\pi/\Omega$ in the direction given by the sign of $|a_{1,1}|^2 - |a_{1,-1}|^2$. That is, assuming the first term is dominant, if the absolute value of the second, counter-clockwise rotating term is greater than that of the third, clockwise rotating one the rotation along the ellipse is positive (counter-clockwise) and vice versa. (If the absolute values are equal the ellipse degenerates to a segment.) In (8) the whole figure rotates with angular frequency ω. The instantaneous angular frequency of $z(t)$ is given by the derivative of the phase $\varphi = \arg(z(t))$. It is now easily seen that, if the rotation around the ellipse is positive, the instantaneous frequency at the maximum of the instantaneous amplitude, when the modulus $|z(t)|$ is maximal, will be higher than ω and vice versa for a negative rotation. The difference will be roughly proportional to Ω multiplied by the ratio of the ellipse dimension over the modulus of the dominating term $a_{1,0}$. More accurately, for $a_{1,-1} = 0$, we would have $\mathrm{d}\varphi/\mathrm{d}t|_{max} = \Omega|a_{1,1}|/|a_{1,0}|$. The frequency shift is thus roughly proportional to the depth of the modulation. For the values presented above the instantaneous angular frequency is plotted in the figure 12(*b*). In figure 12(*c*), the real part of (8) is given to illustrate that, in our case, the maximum of the amplitude corresponds to the maximum of the frequency.

Let us go back to the simulated signals, frequencies and spectra in figures 9, 10 and 11. In parts (*b*) and (*c*) (points 8 and 7) the maximum instantaneous frequency corresponds roughly to the maximum of the amplitude because the dominant frequency at these points is $St_{sym} - St^{(2)}$ whereas the secondary peak corresponding to St_{sym} has a higher frequency. At point 9 (part *a*) the main peak is at St_{sym}, the second highest peak is at $St_{sym} - St^{(2)}$, i.e. at a lower frequency. As the result, the maximum instantaneous frequency in figure 11(*a*) corresponds to the minima of the amplitudes in figure 9(*a*).

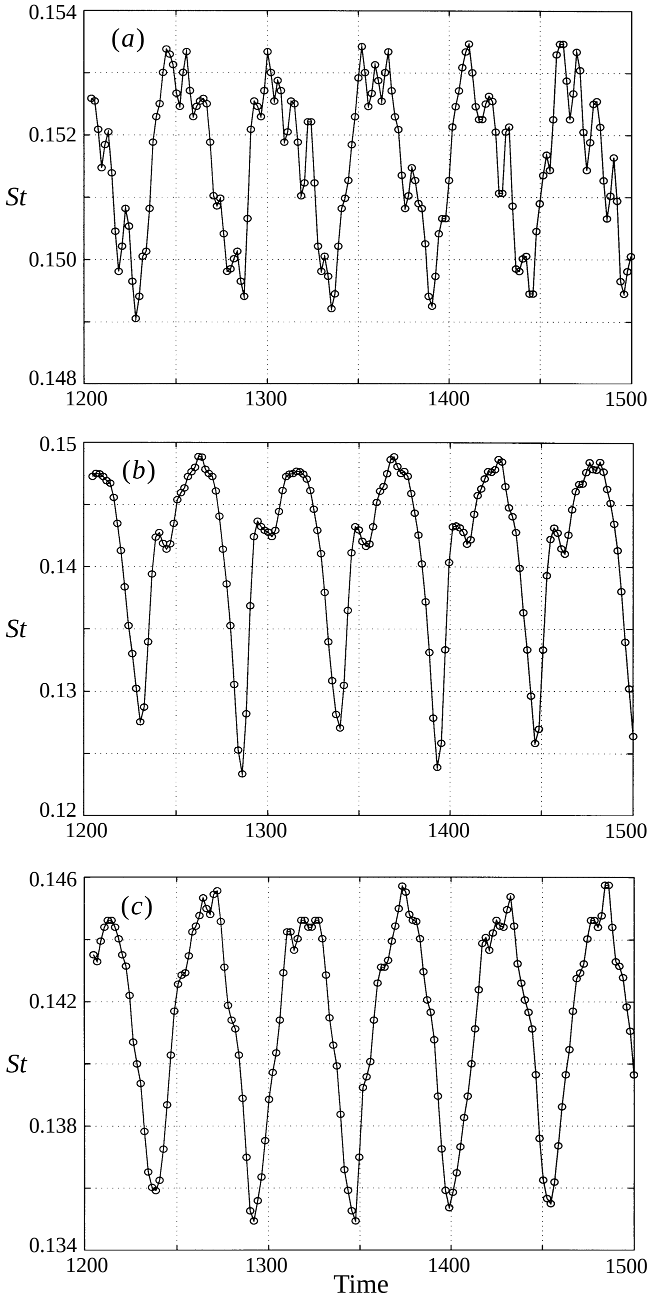

FIGURE 11. Undimensionalized primary frequency of the signals in figure 9.

This simple analysis shows that the properties of the simulated signal are explainable as a destabilization of the fundamental of the limit cycle found in the previous section by a secondary modulation with angular frequency $\omega^{(2)}$. Two uniform frequencies and spatially variable coefficients in (8) account for spatially variable local oscillation frequencies such as those described in Gaster (1969).

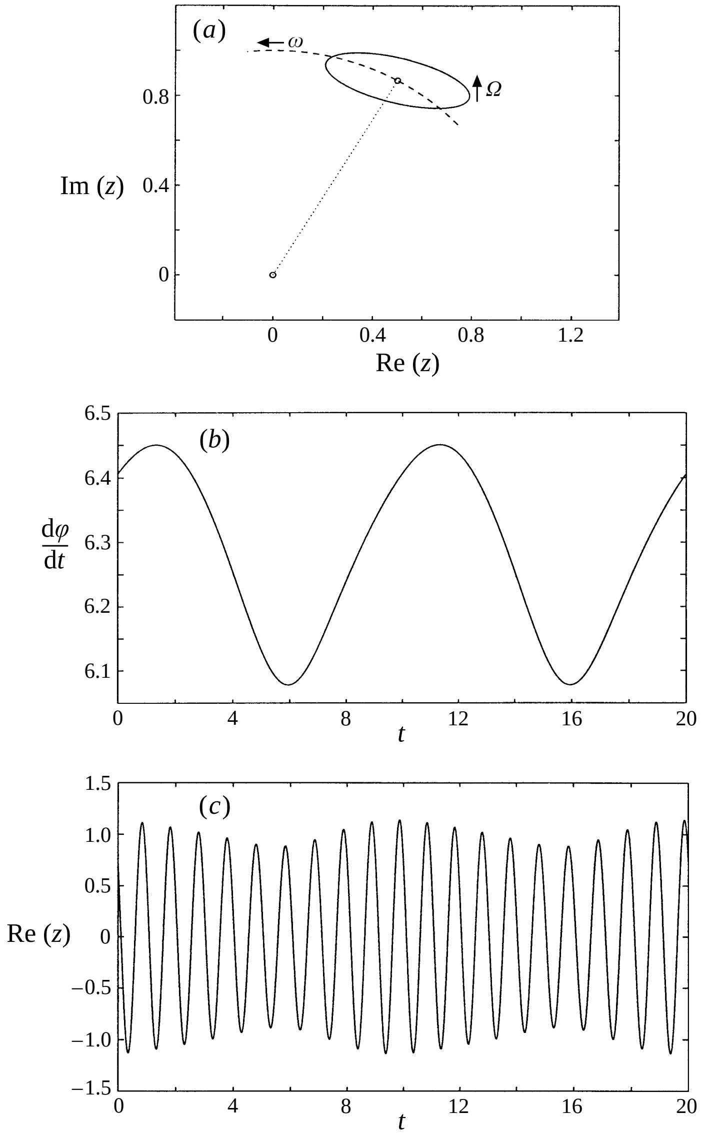

FIGURE 12. (*a*) Complex plot of the expression $a_{1,0}+a_{1,1}e^{i\Omega t}+a_{1,-1}e^{-i\Omega t}$ with $a_{1,0}=e^{i\pi/3}$, $a_{1,1}=0.2e^{i\pi/6}$, $a_{1,-1}=0.1e^{-i\pi/3}$ and $\Omega=0.2\pi$. (*b*) Instantaneous value of the angular velocity of the curve represented in (*a*) rotating with an angular velocity of $\omega=2\pi$. (*c*) The corresponding real value.

5.2. *Destabilization of the limit cycle*

In fact the whole limit cycle becomes unstable. In (4) and (5) the limit cycle has been reduced to a fixed point in the space of Fourier coefficients (1), and analogous pressure Fourier coefficients. Let us denote this primary instability representation

$$\mathscr{R}^{(1)} \equiv \{\boldsymbol{c}_n^{(1)}, d_n^{(1)}\}_{n=-\infty}^{\infty}. \tag{9}$$

In analogy with the primary instability where the transition from a fixed point to a limit cycle could be described by the Fourier series of the velocity–pressure field $\boldsymbol{v}, p$ we can express the transition to the new attractor as a transition from a fixed point defined by the primary Fourier representation $\mathscr{R}^{(1)}$ to

$$\mathscr{R}^{(1)} = \sum_{m=-\infty}^{+\infty} \boldsymbol{r}_m^{(2)} \mathrm{e}^{\mathrm{i}m\omega^{(2)}t}. \tag{10}$$

The Fourier expansion (10) can be written for each Fourier component of the primary instability separately:

$$\boldsymbol{c}_n^{(1)} = \sum_{m=-\infty}^{+\infty} \boldsymbol{c}_{n,m}^{(2)} \mathrm{e}^{\mathrm{i}m\omega^{(2)}t}. \tag{11}$$

The Fourier components $\boldsymbol{c}_n^{(1)}$ being complex, no additional symmetry of the type (3) holds with respect to the m index. Combining the primary and secondary Fourier expansions (1), (11) we arrive at the double Fourier expansion:

$$\boldsymbol{v}(t,.) = \sum_{m=-\infty}^{+\infty} \sum_{n=-\infty}^{+\infty} \boldsymbol{c}_{n,m}^{(2)}(.) \mathrm{e}^{\mathrm{i}n\omega^{(1)}t} \mathrm{e}^{\mathrm{i}m\omega^{(2)}t} \tag{12}$$

and a similar Fourier expansion for the pressure:

$$p(t,.) = \sum_{m=-\infty}^{+\infty} \sum_{n=-\infty}^{+\infty} d_{n,m}^{(2)}(.) \mathrm{e}^{\mathrm{i}n\omega^{(1)}t} \mathrm{e}^{\mathrm{i}m\omega^{(2)}t} \tag{13}$$

allowing, again, the Navier–Stokes equations to be reduced to a system of steady equations:

$$\left(-\nu\nabla^2 + \mathrm{i}n\omega^{(1)} + \mathrm{i}m\omega^{(2)}\right) \boldsymbol{c}_{n,m}^{(2)} + \sum_{k=-\infty}^{+\infty} \sum_{\ell=-\infty}^{+\infty} \boldsymbol{c}_{k,\ell}^{(2)} \cdot \nabla \boldsymbol{c}_{n-k,m-\ell}^{(2)} + \nabla d_{n,m}^{(2)} = 0 \tag{14}$$

with the incompressibility conditions

$$\nabla \cdot \boldsymbol{c}_{n,m}^{(2)} = 0. \tag{15}$$

The fact that the velocity vector and pressure are real now implies

$$\overline{\boldsymbol{c}_{n,m}^{(2)}} = \boldsymbol{c}_{-n,-m}^{(2)}, \quad \overline{d_{n,m}^{(2)}} = d_{-n,-m}^{(2)}. \tag{16}$$

It remains to find first the right angular frequency $\omega^{(1)}$ (or non-dimensionalized frequency $St^{(1)}$) and, secondly, to see whether the curve defined by (12) and (13) reduces to a new limit cycle or whether it fills a T^2-torus.

5.3. *Supercritical primary frequency*

The model (8) indicates how to extract the ratio of the frequency of the basic oscillations and that of their modulation from the direct simulation. The angular frequency of the rapid oscillations in figure 12(*c*) is equal to the total angle along the dashed circle in figure 12(*a*) turned during one full revolution along the ellipse divided by the corresponding time. A quite accurate way to estimate the ratio of both frequencies is to count the number of rapid oscillations for a certain number of slow modulations improving the result by estimating the not quite finished part of the rapid period by a quadratic interpolation. Consider for example figures 9(*a*) and 9(*c*). Five minima delimiting four beatings are visible in both. In figure 9(*a*) corresponding to point 9 in the symmetry plane we count 58.5 oscillations per 4 beatings, i.e. 14.63 oscillations per beating. The corresponding spectrum shows that the rapid oscillations correspond to what we called temporarily St_{sym}, (symbol f_1 in the figures of spectra).

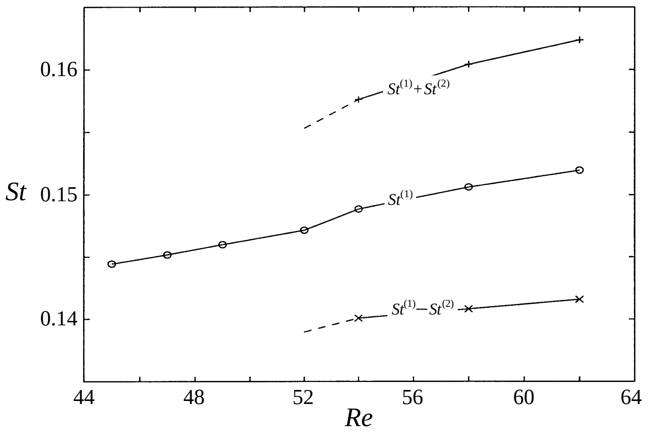

FIGURE 13. Strouhal number of the primary oscillations $St^{(1)}$ *vs.* the Reynolds number under and above the secondary instability threshold ($Re_2 = 53$) in the wake of the finite circular cylinder. At supercritical Reynolds numbers the curves corresponding to $St^{(1)} + St^{(2)}$ and to $St^{(1)} - St^{(2)}$ have been plotted. Their extrapolation to $Re = 52$ is a result of an actual simulation (see the text). ($L/d = 21.4$.)

As a result we find $St_{sym}/St^{(2)} = 14.63$. In contrast, in figure 9(*c*), obtained at point 7 downstream of the cylinder end, we find only 54.7 oscillations per modulation period which yields a ratio of 13.67 periods per modulation. Here, however, the frequency of rapid oscillations is no longer St_{sym} but $St_{sym} - St^{(2)}$ as shown in figure 10(*c*) (the peak labelled '$f_1 - f_2$'). $(St_{sym} - St^{(2)})/St^{(2)} = 13.67$ and so we find now $St_{sym}/St^{(2)} = 14.67$ which is, within the errors of the estimation used, the same ratio as that found at point 9.

Having shown that the same frequency ratio can be recovered independently of the point at which we analyse the signal, we have to make sure that St_{sym} and not, perhaps, $St_{sym} \pm St^{(2)}$ is the right frequency $St^{(1)}$. To see this it is sufficient to make sure that this frequency evolves in a continuous way from the primary instability frequency obtained at Reynolds numbers below the secondary instability threshold. In figure 13 we plot seven Strouhal number values obtained from our simulations in the symmetry plane ($z = 0$). Four of them ($Re = 45, 47, 49, 52$) correspond to Reynolds numbers below the secondary instability threshold where only one frequency is present in the wake. At $Re = 54$, 58 and 62 we plot the $St^{(1)}$ values identified as St_{sym} above. To make it clear that no ambiguity can arise we also plot the values $St^{(1)} \pm St^{(2)}$. The subcritical value of $St^{(2)}$ at $Re = 52$ (dashed lines) could be obtained from the signal in figure 7(*b*). The modulation vanishes more slowly than numerical transients, is clearly visible and its frequency can be roughly estimated. We can see that only the $St^{(1)}$ curve can be considered continuous. The unambiguous determination of the right supercritical $St^{(1)}$ value is due to the Hopf-like character of the secondary bifurcation with its non-zero critical frequency. We thus confirm rigorously the known experimental fact that, for low Reynolds numbers (close to the onset of the vortex shedding), the right Strouhal number yielding a continuous Roshko law is that originating from the symmetry plane of the flow (Gerich & Eckelmann 1982), where the main frequency $St^{(1)}$ dominates in the widest Reynolds number interval.

The difference due to the addition or subtraction of $St^{(2)}$ clearly dominates the kink visible on the $St^{(1)}$ curve in figure 13 at the critical Reynolds number value of 53. This kink is not explainable by numerical errors of processing of the simulated

Reynolds number	52	54	58	62	100
$St^{(1)}/St^{(2)}$	≈ 18	16.97	15.36	14.63	≈ 10

TABLE 2. Values of the primary-to-secondary frequency ratio for a varying Reynolds number and $L/d = 21.4$. The values for $Re = 52$ and $Re = 100$ are estimates. At the subcritical Reynolds number value of 52 the flow is transient, at $Re = 100$ the estimate is obtained from an imperfectly reached limit torus.

data and is of physical nature. It can be interpreted as the shift of the primary instability frequency due to the secondary instability development. The value of $St^{(1)}$ at $Re = 52$ corresponds to very small amplitudes of the secondary instability and can be considered as that of the unperturbed primary instability, whereas that plotted at $Re = 54$ corresponds already to the asymptotic state at the limit torus (saturated secondary instability).

5.4. *Incommensurate frequencies*

To prove that the attractor is not just a new limit cycle but really a torus it has to be shown that the values $St^{(1)}$ and $St^{(2)}$ (or $\omega^{(1)}$ and $\omega^{(2)}$) are incommensurate. This would be hard to prove rigorously for one fixed Reynolds number value. Moreover and more importantly, it has to be shown that in a wide interval of Reynolds number values the frequencies do not 'lock in' with a fixed rational ratio. The simulations for a varying Reynolds number yield a ratio $\omega^{(1)}/\omega^{(2)}$ decreasing continuously with the Reynolds number (table 2).

Note the good agreement of the values in table 2 with the '4-group mode' prediction of Sirovich (1985) obtained by a very simple theory based merely on such classical experimental laws valid for the infinite cylinder as the Roshko law and the drag *vs.* Reynolds number dependence. For $Re = 58$ the inverse ratio $\omega^{(2)}/\omega^{(1)}$ given by Sirovich (1985) is 0.064 which is to be compared to our $1/15.36 = 0.065$. Also the remaining values fall very close to the curve of figure 4 of Sirovich (1985).

No lock-in trend exists. The toroidal topology of the attractor can, of course, be illustrated by plotting a Poincaré section of the manifold described in three dimensions by the three velocity components at a fixed point of the flow (figure 14). An extremely long simulation would be necessary to obtain a really continuous section.

6. Spatial description of the secondary instability T^2-torus

6.1. *Computation of the Fourier modes*

In the same way as for a limit cycle, the full spatial description of the limit torus of the secondary instability is given by complex functions of space representing the coefficients of its double Fourier decomposition (12). The direct Navier–Stokes solution yields the torus only in the limit of an infinitely long simulated time when the whole T^2-surface is filled by the flow trajectory. As a consequence a finite computer run can provide only an approximation. We shall limit ourselves to presenting only the main Fourier components $n = 0, \pm 1$ and $m = 0, \pm 1$ of the development (12), i.e. the mean value and the fundamental of the primary and secondary instability. These are obtainable with a sufficient accuracy by analysing the flow over only one secondary instability period because of the rather high

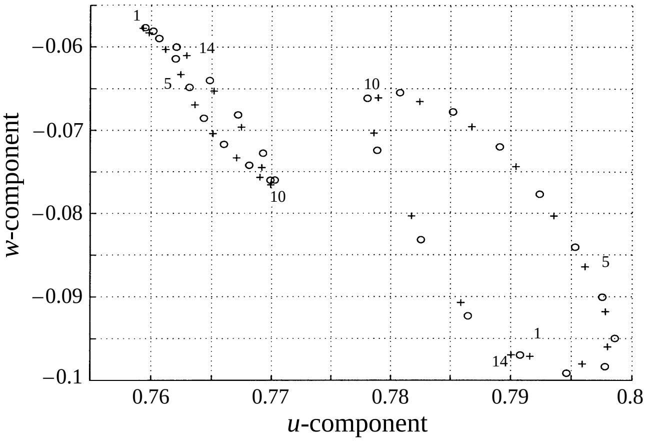

FIGURE 14. Poincaré section obtained by plotting the intersections of the velocity vector at point 6 ($x = 3.5, y = -0.29, z = 5.9$) at $Re = 62$ with the $v = 0$ plane. Both the descending and ascending sections are plotted over two periods (circles and crosses) of the secondary instability. ($L/d = 21.4$.) The crosses numbered 1, 5, 10 and 14 mark, respectively, the first, fifth, tenth and fourteenth intersection with the $v = 0$ plane.

value of the primary to secondary instability frequency ratio at low Reynolds numbers.

The spatial analysis presented in this section concerns the circular cylinder wake at $Re = 54$. At this Reynolds number the ratio of the frequencies $\omega^{(1)}/\omega^{(2)}$ is about 17. We can therefore consider the factor $e^{im\omega^{(2)}t}$ in the Fourier expansion (12) as constant over one period $T^{(1)} = 2\pi/\omega^{(1)}$ of the rapid oscillations as long as the harmonic m considered is low. Moreover, less than 2% above the threshold, the fundamental of the secondary instability largely dominates higher harmonics. As a consequence, the error of the mean value and of the primary fundamental computed over the period $T^{(1)}$ can be estimated not to exceed 10%. On the basis of these considerations we proceeded in the following way. We kept the on-line processing algorithm presented in §3 above the secondary instability threshold. The 'time clock' for the period determination was still based on the v-velocity oscillations at a point in the symmetry plane (point 9 of table 1). At this point, so close to the secondary instability threshold, the period fluctuations are insignificant (0.35%): the 'instantaneous' period computed at this point is thus quite accurately $T^{(1)}$.

The primary instability Fourier coefficient integration was triggered for a number of successive periods covering one secondary instability period $T^{(2)} = 2\pi/\omega^{(2)}$, i.e. more than 17 in this case, and the space fields of the coefficients $\boldsymbol{c}_n$ for $n = -2, -1, 0, 1$ and 2 were stored at each period $T^{(1)}$. The complex fields obtained vary in time over one secondary instability period and represent the destabilized primary limit cycle. They can be considered as discretized values of instantaneous primary instability Fourier coefficients and the secondary Fourier analysis (11) can be applied to them. (Actually only the mean value, $m = 0$, and the first harmonic, $m = \pm 1$, were computed.) If we limit ourselves to $|m| \leqslant 1$ and $|n| \leqslant 1$ and disregard the pressure Fourier coefficients we obtain 12 independent complex functions corresponding to $(n, m) = (1, 0), (0, 1), (1, 1)$ and $(1, -1)$ and three real functions corresponding to the mean value $n = 0$, $m = 0$ (three components u, v and w for each pair of Fourier expansion indices). In what follows we present some of their most important aspects.
]

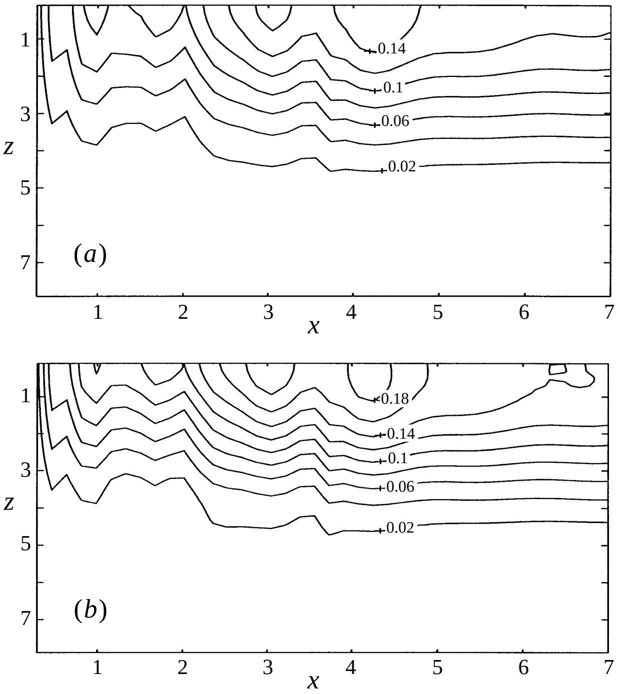

FIGURE 15. (*a*) Comparison of the iso-amplitude plot of the transverse (v) velocity component fundamental $c_{v,1}$ in the plane containing the cylinder axis below the secondary instability threshold ($Re = 49$) and (*b*) of the mean fundamental $c_{v,1,0}$ above the secondary instability threshold ($Re = 54$). ($L/d = 21.4$.)

6.2. *Mean limit cycle* ($m = 0$)

The Fourier modes with $m = 0$ are the mean values of the primary instability Fourier harmonics over one beating. They can be considered as describing the average limit cycle and are a continuation of the subcritical Fourier harmonics in the same way as the mean flow evolves continuously from the steady subcritical flow at the primary bifurcation. As a result, the (real) vector $\boldsymbol{c}_{0,0}$ describing the mean flow is still similar to the primary instability mean flow (and the subcritical steady flow) and also the mean fundamental $\boldsymbol{c}_{1,0}$ is expected to be very similar to $\boldsymbol{c}_1$ obtained at $Re < Re_2$ in §3 (figures 4–6). This is, indeed, the case as can be seen if the mean primary instability fundamental $c_{v,1,0}$ at $Re = 54$ is compared to the subcritical fundamental $c_{v,1}$ (figure 15). The similarity of the plots in figure 15 provides additional proof of the correctness of the continuation of the primary instability frequency $St^{(1)}$ above the secondary instability threshold because if we had based our decomposition on, say, $St^{(1)} - St^{(2)}$ we would have found significantly different shapes (see figure 17).

6.3. *Secondary-instability fundamental harmonic*

The amplitude envelopes of oscillations arising due to the secondary instability are represented in figures 16 and 17. At the secondary instability the mean values over one primary period $1/St^{(1)}$ start to oscillate with the frequency $St^{(2)}$. The envelopes of oscillations of the streamwise velocity component u (i.e. the modulus of the Fourier mode $c_{u,0,1}$) are plotted in figure 16. The figure 16(*a*) shows a distinct maximum of the represented Fourier mode at $z = 3$ (halfway between the symmetry plane and

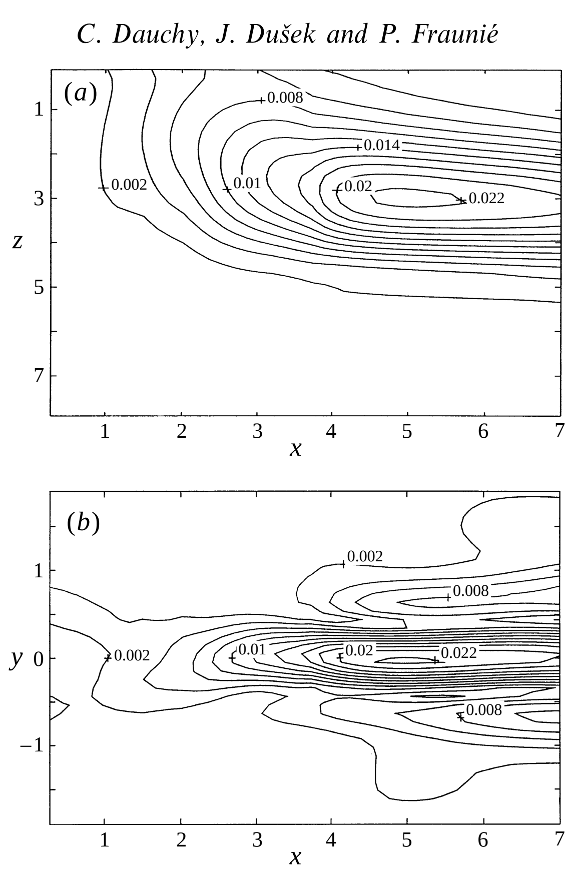

FIGURE 16. Iso-amplitude plot of the oscillations of the streamwise velocity at the frequency $St^{(2)}$ (modulus of the Fourier mode $c_{u,0,1}$). (*a*) The plane containing the cylinder axis, (*b*) the plane $z = 3$ normal to the cylinder axis.($Re = 54$, $L/d = 21.4$.)

cylinder end). The transverse structure (figure 16*b*) of the mode is similar to that of the mean velocity correction observed at the primary instability in the cylinder wake (Dušek 1996). The same spanwise structure as in figure 16 is obtained for the spanwise velocity oscillations at the same frequency or if the amplitude envelope of the transverse velocity oscillations at the $St^{(2)}$ frequency (modulus of the mode $c_{v,0,1}$) is represented in the $y = 0.5$ plane. (This Fourier mode is antisymmetric with respect to the $y = 0$ plane and so a plane $y \neq 0$ has to be chosen.) For all three velocity components of the Fourier mode $n = 0$, $m = 1$ a maximum situated between $z = 3$ and $z = 4$ is observable.

The Fourier mode $c_{v,1,-1}$ describes the lateral peak of the primary fundamental shown to be responsible for the experimentally observed continuous spanwise evolution of the 'local' frequency from $St^{(1)}$ to $St^{(1)} - St^{(2)}$ (see §5). To have an accurate reference we plot, in figure 18, the spectra obtained at $Re = 54$ at the same points as in figure 10 where they correspond to $Re = 62$. Except that the lateral peak $St^{(1)} - St^{(2)}$ at points 8 and 7 (parts *b* and *c*) does not yet dominate the principal peak $St^{(1)}$ because we are still close to the instability threshold, the spanwise trend is the same. It can be compared to the spanwise structure shown in figures 15 (*b*) and 17. Points 9, 8 and 7 corresponding to figure 18(*a–c*) lie along the $x = 3.5$ line, approximately in the $y = 0$ plane at $z = 0$, $z = 3.2$ and $z = 5.9$, respectively. Whereas the main peak $St^{(1)}$ decreases monotonically from a value exceeding 0.1 at the point

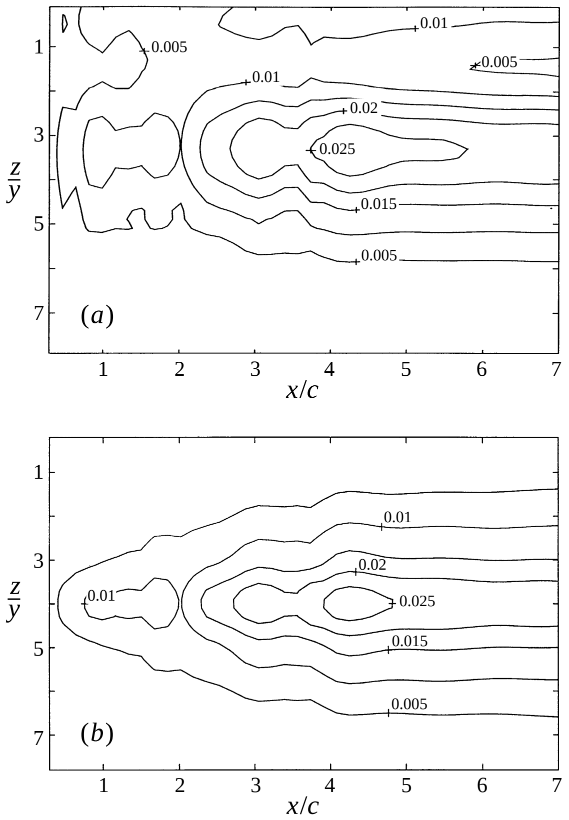

FIGURE 17. Iso-amplitude plot of the oscillations of the transverse velocity at the frequency $St^{(1)} - St^{(2)}$ (modulus of the Fourier mode $c_{v,1,-1}$) (*a*) in the plane containing the cylinder axis, (*b*) in the plane $z = 3$ normal to the cylinder axis and passing through the mode maximum. ($Re = 54$, $L/d = 21.4$).

in the symmetry plane (figure 18*a*) to about 0.04 downstream of the cylinder end (figure 18*c*) the lateral peak $St^{(1)} - St^{(2)}$ is about twice as high in the figure 18(*b*) (point halfway between the symmetry plane and the cylinder end) than in figure 18(*a*), ($z = 0$). The decrease towards the cylinder end is then, much slower than for the main peak so that in figure 18(*c*) both peaks are almost equal and, in figure 10, obtained higher above the threshold, the lateral peak dominates. The height of the peaks in the spectra in figure 18 corresponds quite well to the global spatial plots of figures 15 and 17. A slight underestimation is due to the limited resolution of the spectra. In contrast, the lateral peak $St^{(1)} + St^{(2)}$ has a monotonically decreasing trend in the spanwise direction identical to that of the main peak so that the ratio of both (roughly 10) remains practically constant. Indeed, the space plot of the spanwise space structure of the envelope $|c_{v,1,1}|$ (not represented) is qualitatively the same as in figure 15. The comparison of spectra in figures 10 and 18 and of the envelopes of Fourier modes $n = 1, m = 0$ (figure 15) and $n = 1, m = -1$ (figure 17) also allows the trend due to an increasing Reynolds number to be understood. The side mode $n = 1, m = -1$ becomes progressively stronger than the main mode $n = 1, m = 0$ in a wider spanwise zone of the wake, which accounts for the widening of the ‘affected’ zones downstream of the cylinder ends. Ultimately the central zone may disappear and the lower frequency $St^{(1)} - St^{(2)}$ may dominate.

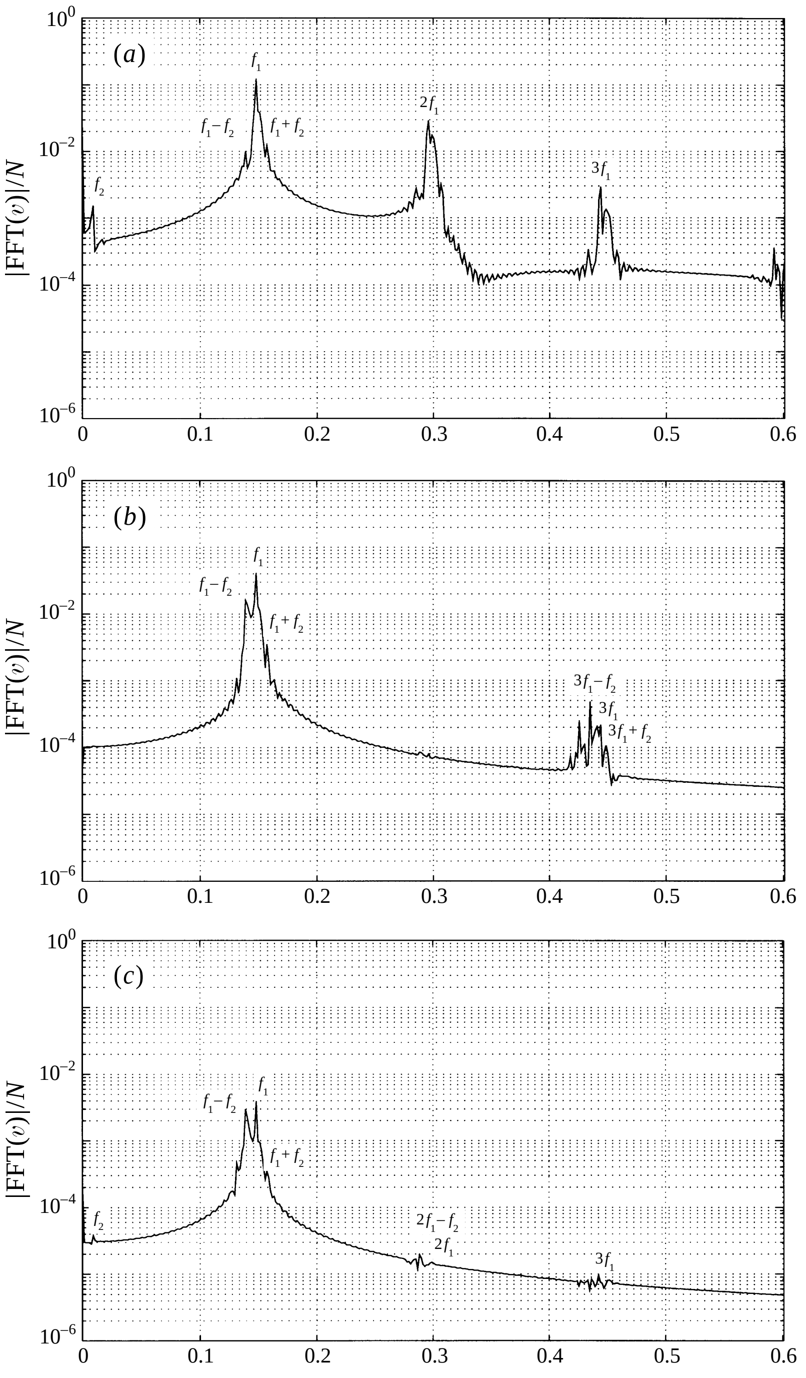

FIGURE 18. Spectra – absolute values of the Fourier transforms of v-velocity oscillations at $Re = 54$ ($L/d = 21.4$) at the same points as in figure 10(a): at a point in the symmetry plane ($x = 3.5, y = -0.3, z = 0$), (b) a point halfway between the symmetry plane and the cylinder end in the spanwise direction ($x = 3.5, y = 0, z = 3.2$) and (c) a point downstream of the cylinder end ($x = 3.5, y = 0, z = 5.9$). See also caption of figure 10.

Fourier mode	Strouhal number St	k_x (in d^{-1}, d is cylinder diameter)	Phase velocity $2\pi St/k_x$
$c_{u,0,1}$	0.00876	0.050	1.1
$c_{w,0,1}$	0.00876	0.043	1.3
$c_{v,1,0}$	0.14866	0.966	0.96
$c_{v,1,-1}$	0.13990	0.912	0.96

TABLE 3. Wavenumbers and phase velocities near the domain outflow for several Fourier modes of the limit torus at $Re = 54$ and for the cylinder of aspect ratio $L/d = 21.4$.

The maxima of the Fourier modes $n = 0, m = 1$ and $n = 1, m = -1$ described above lie in the zone of the velocity deficit due to the flow recirculation around the cylinder end. This deficit is visible in figure 2(*b*) plotted at $Re = 49$. The unperturbed 'basic' flow of the secondary instability at the slightly higher Reynolds number of $Re = 54$ would be almost identical due to the small Reynolds number difference. As the result, the secondary instability can be associated with this velocity deficit maximum in the spanwise direction in the same way as the primary instability is associated with the velocity deficit in the transverse direction.

6.4. *Wavelength of the secondary-instability fundamental harmonic*

It has been shown (Dušek 1996) that the primary-instability Fourier harmonics behave asymptotically like plane waves with wavenumbers proportional to their order. It means that all the harmonics have asymptotically the same phase velocity. Although the extent of the domain considered in this simulation does not really provide access to the far-wake characteristics it can been seen whether the primary and secondary instabilities have a common phase velocity, i.e. whether the ratio of their wavenumbers is roughly equal to the ratio of their frequencies. If this is the case the secondary instability has to be expected to have an extremely long wavelength. At $Re = 49$ the primary-instability fundamental wavelength seen in figure 6 is roughly equal to 3.3, i.e. 5.8 cylinder diameters. Assuming that at $Re = 54$ it is only slightly shorter and taking into account the ratio $St^{(1)}/St^{(2)}$ of about 17 the expected secondary instability wavelength of about 100 cylinder diameters greatly exceeds the computational domain length.

In spite of this fact, the wavenumber can easily be computed as the phase gradient. Along the flow axis ($y = 0, z = 0$), its only non-zero component is $k_x = \partial\varphi/\partial x$ and this component is also the most significant elsewhere except very close to the cylinder. To investigate simultaneously the primary and secondary instability wavelengths we computed k_x along the line $z = 3$, $y = 0$ for the Fourier modes $c_{u,0,1}$, $c_{w,0,1}$ (fluctuations of the primary-instability mean values of the u- and w-velocity components) and for $c_{v,1,0}$ and $c_{v,1,-1}$ (Fourier modes corresponding to the frequencies $St^{(1)}$ and $St^{(1)} - St^{(2)}$). The streamwise wavenumber (k_x) values near the domain outflow are presented in table 3. The agreement with expectation is quite satisfactory. In particular, the phase velocity values for the slowly oscillating modes $c_{u,0,1}$ and $c_{w,0,1}$ represent a good test taking account of the small values of the corresponding wavenumbers. It is also satisfactory to find the difference of the wavenumbers of Fourier modes $c_{v,1,0}$ and $c_{v,1,-1}$ (0.054 d^{-1}) comparable to the wavenumbers of the slow modes $c_{u,0,1}$ and $c_{w,0,1}$. The value of the phase velocity slightly smaller than one is in agreement with two-dimensional simulations (Dušek 1996) and experimental measurements for a cylinder with a high aspect ratio (Williamson 1989) at comparable Reynolds numbers.

The secondary-instability wavelength is experimentally observable on the streamwise modulation of the vortex shedding pattern. It can be associated with the streamwise lengthscale of the vortex splitting at the limit of the affected and unaffected zones visible in figure 2 of Eisenlohr & Eckelmann (1989).

6.5. *Spatial structure of the Fourier modes and wake observations*

We have already said that not only the 'mean' Fourier modes $\boldsymbol{c}_{n,0}$ but also the harmonics of oscillations of the 'mean value' $\boldsymbol{c}_{0,m}$ have the same shape of envelopes in the transverse ($z = \text{const}$) planes as their primary homologues $\boldsymbol{c}_n$ and $\boldsymbol{c}_0$. This seems to be the case, more generally, for any n and m, i.e. the transverse shape of the Fourier mode envelopes of $\boldsymbol{c}_{n,m}$ is similar to that of the nth primary instability harmonic. As the result, the secondary instability can be interpreted as a splitting of the primary harmonics into a series of secondary harmonics each having the transverse structure of the primary one. The analysis of the flow oscillations at the primary frequencies $(n, 0)$ as well as at the secondary one (n, m) yields the same transverse picture of the wake, which explains why the switching from one to another does not change the observed transverse wake structure. In contrast, the spanwise structure of some secondary Fourier modes is different from that of the primary modes. Whereas the primary Fourier mode $n = 1$ below the secondary-instability threshold as well as its 'mean' ($n = 1, m = 0$) above the threshold (figure 16) reach their maximum in the $z = 0$ symmetry plane and decay progressively towards the cylinder ends, modes arising due to the secondary instability onset (e.g. $n = 0$, $m = 1$ in figure 17, or $n = 1$, $m = -1$ in figure 18) have a maximum off the symmetry plane (about half the distance between the symmetry plane and the cylinder end). For this reason, in the proximity of the symmetry plane $z = 0$ the primary fundamental Fourier mode (1,0) dominates, whereas farther from this plane it is overshadowed by the secondary one $(1, -1)$.

This effect may be explained by the trend to lower frequencies toward the ends of the obstacle. It is not necessary for the cylinder end to be tapered to think of the argument of Gaster (1969) concerning slender cones. The molecular diffusion smooths the sudden diameter variation at the cylinder end and a shallower wake with a similar transverse structure exists even off the cylinder span (see figure 5). For real cones this trend may make several lower frequency modes $m = -1, -2, \ldots$ progressively dominate. As a result the idea of Gaster that lower frequencies are to be associated with local Reynolds numbers is qualitatively right except that the phenomenon occurs in a discrete way, as confirmed by later observations for cones (König 1993) as well as for cylinders (e.g. König *et al.* 1993).

6.6. *Description of the transition to a limit torus*

In Carte *et al.* (1995, 1996) a mathematical formulation to compute the transition to a limit cycle starting from an arbitrary initial condition has been given. In two dimensions it has even been shown that the formulation presented provides an efficient computing method (Carte *et al.* 1995). A similar formulation can be written for the limit torus and can be expected to provide a tool for a direct computation of its Fourier modes as well as for the transients characterizing the decay of the primary limit cycle.

Consider initial double Fourier expansions of the type (12) and (13) with time-dependent Fourier coefficients and time-dependent angular frequencies ω_1 and ω_2:

$$\boldsymbol{v}(t, .) = \sum_{m=-\infty}^{+\infty} \sum_{n=-\infty}^{+\infty} \boldsymbol{c}_{n,m}(t, .) \mathrm{e}^{\mathrm{i}n\omega_1 t} \mathrm{e}^{\mathrm{i}m\omega_2 t} \tag{17}$$

and

$$p(t,.) = \sum_{m=-\infty}^{+\infty} \sum_{n=-\infty}^{+\infty} d_{n,m}(t,.)\mathrm{e}^{\mathrm{i}n\omega_1 t}\mathrm{e}^{\mathrm{i}m\omega_2 t}. \tag{18}$$

By the same reasoning as in Carte *et al.* (1995) it can be shown that this expansion satisfies the Navier–Stokes equations if its coefficients satisfy the system of unsteady equations

$$\frac{\partial \boldsymbol{c}_{n,m}}{\partial t} + \left(-\frac{1}{Re}\nabla^2 + \mathrm{i}n\omega_1 + \mathrm{i}m\omega_2\right)\boldsymbol{c}_{n,m} + \sum_{k=-\infty}^{+\infty}\sum_{\ell=-\infty}^{+\infty} \boldsymbol{c}_{k,\ell}\cdot\nabla\boldsymbol{c}_{n-k,m-\ell} + \nabla d_{n,m} = 0, \tag{19}$$

$$\nabla\cdot\boldsymbol{c}_{n,m} = 0. \tag{20}$$

If the limit torus is approached and the angular frequencies do not have the right instantaneous values the differences between the right values and those appearing in (17), (18) and (19) will yield, in general, a biperiodic movement of the Fourier coefficients in the complex plane. However, the Fourier modes $n = 1, m = 0$ and $n = 0, m = 1$ will simply rotate, their angular frequency corresponding to the difference between the exact and used values of ω_1 and ω_2, respectively. The angular frequencies of the double Fourier expansion can then be updated using analogous constraints as in the limit cycle case. We can require for example that

$$\frac{\partial}{\partial t}\left[\frac{c_{1,0,v}(t,\vec{x}_1)}{|c_{1,0,v}(t,\vec{x}_1)|}\right] = 0, \tag{21}$$

and

$$\frac{\partial}{\partial t}\left[\frac{c_{0,1,u}(t,\vec{x}_2)}{|c_{0,1,u}(t,\vec{x}_2)|}\right] = 0, \tag{22}$$

i.e. that selected components of the mode $n = 1, m = 0$ at a fixed point x_1, chosen near the primary-instability maximum, and of the mode $n = 0, m = 1$ at a point x_2, chosen near the secondary-instability maximum, do not rotate in the complex plane and use these constraint for updating the angular frequencies ω_1 and ω_2. The system (19)–(22) becomes steady on the torus and describes the transition from a fairly arbitrary initial condition, not too distant from the attractor, to the limit torus.

7. Aspect ratio influence

To estimate the trends associated with the change of the aspect ratio of the obstacle we carried out simulations, in very similar conditions, for a cylinder with half the aspect ratio, $L/d = 10.7$. A full domain was used to test, at the same time, the symmetry with respect to the $z = 0$ plane.

Simulations at Re=62, 80 and 100 have been run. For the first two Reynolds numbers values the wake has been found monoperiodic; only at $Re = 100$ has the onset of the secondary instability been observed, allowing the secondary critical Reynolds number to be put roughly at $Re_2 = 90$, which is considerably higher than for the cylinder with twice the aspect ratio.

To provide a good basis of comparison a simulation on the cylinder with $L/d = 21.4$ at $Re = 100$ has also been made.

The comparison of primary Strouhal numbers $St^{(1)}$ for both configurations at $Re = 62$ and $Re = 100$ as well as of secondary Strouhal numbers $St^{(2)}$ at $Re = 100$ is given in table 4. The Roshko law (Roshko 1954) applied to the modulation frequency

	Re_2	$St^{(1)}\|_{Re=62}$	$St^{(1)}\|_{Re=100}$	$St^{(2)}\|_{Re=100}$	$St^{(1)}/St^{(2)}\|_{Re=100}$
$L/d = 21.4$	53	0.1520	0.1646	≈ 0.016	≈ 10
$L/d = 10.7$	≈ 90	0.1472	0.1476	0.01287	11.47

TABLE 4. Comparison of the primary and secondary Strouhal numbers for cylinders with $L/d = 21.4$ and $L/d = 10.7$

f and the spanwise length L of the cylinder would suggest that a Reynolds number UL/v based on the cylinder length, the inflow velocity U and the viscosity v should yield a practically constant Strouhal number fL/U at the diameter-based Reynolds numbers and aspect ratios considered here. As a result, a modulation frequency f inversely proportional to the aspect ratio would be expected. As pointed out by Gaster (1969), instead a proportionality law between fL/U and UL/v holds, giving a modulation frequency independent of the aspect ratio is obtained. The trend found (see table 4) lies somewhere in between. A slight trend of the secondary-instability frequency to decrease if the diameter based-Reynolds number is fixed and the aspect ratio increases seems to exist but is weaker than what the Roshko law would predict.

The primary Strouhal numbers found at $Re = 62$ and $Re = 100$ show that the shorter the cylinder the flatter the Strouhal *vs.* Reynolds number dependence. Actually the longer cylinder with L/d=21.4 yields a significantly smaller variation $\Delta St/\Delta Re = 3.3 \times 10^{-4}$ than for an infinite configuration ($\Delta St/\Delta Re = 6.4 \times 10^{-4}$ in the same Reynolds number range – see Williamson 1989). The variation obtained for $L/d = 10.7$ appears to be quite insignificant. For a given, significantly supercritical, Reynolds number this trend results in a significant decrease of the primary Strouhal number (see the values of $St^{(1)}$ at $Re = 100$ in table 4). This seems to be in agreement with experimental observation (Gerich & Eckelmann 1982).

The data obtained by simulation do not allow one to see accurately if the aspect ratio influences the primary to secondary frequency ratio $St^{(1)}/St^{(2)}$. The very approximate estimation made at $Re = 100$ for the larger aspect ratio indicates that the difference if any is likely to be very small. This would be in agreement with the theory of Sirovich (1985) mentioned already in §5.4. For both aspect ratios considered the infinite cylinder experimental laws used by Sirovich remain valid and a practically aspect-ratio-independent value of $St^{(1)}/St^{(2)}$ is thus to be expected. This conclusion seems to be supported, moreover, by the fact that the well-established ratio $St^{(2)}/St^{(1)} = 1/11.47 = 0.087$ obtained for L/d=10.7 at $Re = 100$ (see table 4) is quite close to the curve of '4-group mode' of Sirovich (1985).

The level of the primary instability for both aspect ratios at comparable Reynolds numbers does not differ very much either. Table 5 shows that the oscillation amplitude (its mean value for cases where the secondary instability has developed) is practically the same for both aspect ratios at corresponding positions obtained by rescaling the z-axis with respect to the cylinder length. This may be attributed to the fact that the threshold of the primary instability is relatively weakly dependent on the aspect ratio variation considered (Mathis 1983).

A substantial part of previous investigations has been devoted to the spatial aspects of the secondary instability. To provide a rapid comparison of the overall trends we plotted an analogue of figures 10 and 18. In figure 19 the spectra of the v-velocity signals at a point in the symmetry plane $z = 0$ (19*a*) at $L/4$ off this plane (19*b*) and a point downstream of the cylinder end (19*c*) are plotted. The asymmetry of the lateral

	$z = 0$	$z \approx L/4$	$z \approx L/2$
$Re = 62$			
$L/d = 21.4$	0.40	0.23	0.041
$L/d = 10.7$	0.40	0.31	0.083
$Re = 100$			
$L/d = 21.4$	0.53	0.42	0.33
$L/d = 10.7$	0.51	0.47	0.36

TABLE 5. Primary instability amplitudes (average amplitudes of oscillations above the secondary instability threshold) for $L/d = 21.4$ and $L/d = 10.7$ and two different Reynolds number values at three points lying at $x = 3.5, y = 0$ and, respectively, in the symmetry plane $z = 0$ about halfway between the cylinder end and the symmetry plane ($z = 3.2$ for $L = 12$ and $z = 1.3$ for $L = 6$) and downstream of the cylinder end ($z = 5.9$ for $L = 12$ and $z = 2.9$ for $L = 6$).

peaks, and thus the trend to the formation of affected zones is less pronounced. In contrast with the larger aspect ratio (figure 18) the frequency peak $St^{(1)}+St^{(2)}$ is higher than that corresponding to $St^{(1)}-St^{(2)}$. The trend of the lower-frequency peak to vanish more slowly than the higher-frequency one is still visible, but the ratio of the main peak to the lateral ones seems rather to increase with the distance from the symmetry plane.

The presence of the second harmonic in the $y = 0$ symmetry plane (plane containing the cylinder axis) in 19(*b*) and especially in the 19(*c*) observable to a lesser degree also for L/d=21.4 (figures 10*c* and 18*c*) is not physical and is to be attributed to an insufficient resolution at element interfaces. (The plane $y = 0$ corresponds to element interfaces, see figure 1.)

8. Conclusions

The results of our theoretical analysis of the simulation of the three-dimensional wake of a finite cylinder provide an interpretation of some experimentally observed three-dimensional effects in terms of a secondary instability. The description of the finite cylinder wake dynamics in terms of a T^2-torus is not in contradiction with existing observations and provides a theoretical framework for the understanding of most observed phenomena.

A number of interesting questions that could not be tackled in the present paper arise. They are related to the behaviour of wakes of other finite objects. For cones a number of spanwise zones with local dominant frequencies decreasing proportionally to the decrease of the local diameter has been reported (Gaster 1971). These zones have been recognized as characterized by discrete decreasing non-dimensional frequencies (König 1993) which might be described in the notation of the present paper as $St^{(1)} - mSt^{(2)}$ with m increasing towards the cone tip. This would mean that, depending on the form of the obstacle, a certain number of Fourier modes (12) and (13) for $n = 1$ and increasingly negative m become dominant along the cone span. The wake of cylinders with end plates behaves much in the same way as that of cylinders with free ends (Gerich & Eckelmann 1982) although, at first sight, the spanwise velocity profiles are considerably different. The case of cylinders between plates or solid walls should be investigated to see if a similar mechanism, possibly the horseshoe vortices, explains the onset of a secondary instability and beatings. A particularly interesting subject consists of making an exhaustive study of wakes for cylinders or any other objects of variable aspect ratio.

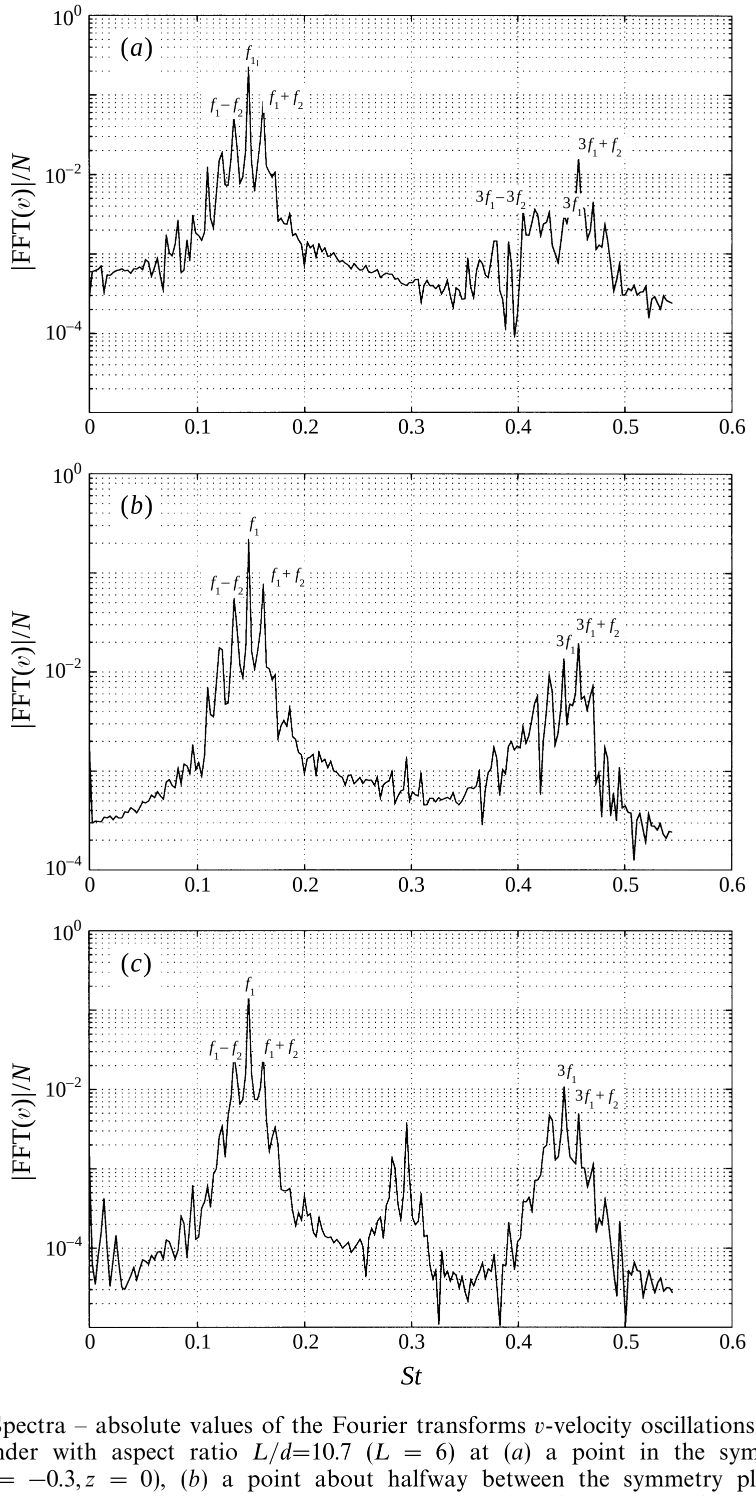

FIGURE 19. Spectra – absolute values of the Fourier transforms v-velocity oscillations at $Re = 100$ for the cylinder with aspect ratio L/d=10.7 ($L = 6$) at (a) a point in the symmetry plane ($x = 3.5, y = -0.3, z = 0$), (b) a point about halfway between the symmetry plane and the cylinder end in the spanwise direction ($x = 3.5, y = 0, z = 1.3$) and (c) a point downstream of the cylinder end ($x = 3.5, y = 0, z = 2.9$). (f_1 stands for $St^{(1)}$ and f_2 for $St^{(2)}$.)

We believe the behaviour analysed in this paper to be typical for early stages of transition to turbulence in the wake of finite objects. The typical Bénard–von Kármán limit cycle characterizing the primary instability is shown to decay, very early for cylinders with large aspect ratio, into a limit torus, explaining the quasi-periodicity observed in the wake. The final transition remains an open question. All that can be said so far is that the chance of a rapid transition to turbulence is quite high in view of the RTN theory (Newhouse *et al.* 1978 and Ruelle & Takens 1971) because only one more subsequent Hopf-like bifurcation of the same type as the secondary one should be expected to yield an unstable attractor. However, a direct transition of the Curry–Yorke type (see Bergé, Pomeau & Vidal 1988) or any other type of decay of the limit torus is possible. It is difficult to investigate these stages of transition by current direct Navier–Stokes solving techniques, in which all effects are superimposed and in which refined data concerning the system dynamics have to paid for by extremely long computer runs. A possible alternative might be a numerical implementation of the direct Fourier mode computation suggested in §6 where the destabilization of the T^2-torus would be made explicit. Our present simulations showed that a qualitatively different dynamics (T^3-torus, turbulence?) sets in at $Re \approx 120$ for the circular cylinder and at $Re \approx 150$ for the NACA wing with the discretization used in this paper.

This work was supported by the French Programme National de Déterminisme du Recrutement. The computations have been performed at the Centre de Ressources Technologiques Mathématiques et Industrielles of the Université de Toulon et du Var.

REFERENCES

Abarbanel, S. S., Don, W. S., Gottlieb, D., Rudy, D. H. & Townsend, J. C. 1991 Secondary frequencies in the wake of a circular cylinder with vortex shedding. *J. Fluid Mech.* **225**, 557.

Albarède, P. & Provansal, M. 1995 Quasi-periodic cylinder wakes and the Ginzburg-Landau model. *J. Fluid Mech.* **291**, 191.

Barkley, D. & Henderson, R. D. 1996 Three-dimensional Floquet stability analysis of the wake of a circular cylinder. *J. Fluid Mech.* **322**, 215.

Benjamin, T. B. & Feir, J. E. 1967 The disintegration of wave trains on deep water. *J. Fluid Mech.* **27**, 417.

Bergé, P., Pomeau, Y. & Vidal, C. 1988 *L'Ordre Dans le Chaos.* Hermann.

Berger, E. 1964 Bestimmung der hydrodynamischen Groessen einer Karmanschen Wirbelstarsse aus Hitzdrahtmessungen bei kleinen Reynoldsschen Zahlen. *Z. Flugwiss.* **12**, 41.

Braza, M., Chassaing, P., Ha Minh, H. 1986 Numerical study and physical analysis of the pressure and velocity fields in the near wake of a circular cylinder. *J. Fluid Mech.* **165**, 79.

Brede, M., Eckelmann, H., König, M. & Noack, B. R. 1994 Discrete shedding modes of the cylinder wake in a jet with homogeneous core. *Phys. Fluids* **6**, 2711.

Carte, G., Dušek, J. & Fraunie, P. 1995 A spectral time discretization for flows with dominant periodicity. *J. Comput. Phys.* **120**, 171.

Carte, G., Dušek, J. & Fraunie. P. 1996 Numerical simulation of the mechanisms governing the onset of the Bénard–von Kármán instability. *Intl J. Numer. Meth. Fluids*, **23**, 753.

Carte, G., Fraunie, P. & Dussouillez, P. 1991 An innovative algorithm for periodic flows calculation using a parallel architecture. Some Applications for unsteady aerodynamics. *Sixth Intl Symp. on Unsteady Aerodynamics, Aeroacoustics and Aeroelasticity of Turbomachines and Propellers, University Notre Dame, USA, Sept. 15-19, 1991*, Springer.

Crawford, J. D. & Knobloch, E. 1991 Symmetry and symmetry-breaking bifurcations in fluid dynamics. *Ann. Rev. Fluid Mech* **23**, 341.

Dauchy, C. 1995 Etude numérique d'une instabilité secondaire dans le sillage de cylindres finis. PhD thesis, IRPHE, Université d'Aix-Marseille II.

Dušek, J. 1996 Spatial structure of the Bénard–von Kármán instability. *Eur. J. Mech.* B *Fluids.* **15**, 619.

Dušek, J. & Fraunie, P. 1993 Validation and error estimate of a spectral element discretization of a cylinder wake. In *Numerical Methods in Laminar and Turbulent Flows'93*, vol. VIII, Part 1 (ed. C. Taylor). Pineridge Press.

Dušek, J., Fraunie, P. & Seror, S. 1994*a* Mise en évidence du doublement de période dans le sillage d'une aile NACA à la deuxième bifurcation de Hopf. *C. R. Acad. Sci. Paris* **319**, II, 1271.

Dušek, J., Le Gal, P. & Fraunie, P. 1994*b* A numerical and theoretical study of the first Hopf bifurcation in a cylinder wake. *J. Fluid Mech.* **264**, 59.

Eisenlohr, H. & Eckelmann, H. 1989 Vortex splitting and its consequence in the vortex street wake of cylinders at low Reynolds numbers. *Phys. Fluids* A **1**, 189.

Gaster, M. 1969 Vortex shedding from slender cones at low Reynolds numbers. *J. Fluid Mech.* **38**, 565.

Gaster, M. 1971 Vortex shedding from circular cylinders at low Reynolds numbers *J. Fluid Mech.* **46**, 749.

Gerich, D. & Eckelmann, H. 1982 Influence of end plates and free ends on the shedding frequency of circular cylinders. *J. Fluid Mech.* **122**, 109.

Goujon-Durand, S., Jenffer, P. & Wesfreid, J. E. 1994 Downstream evolution of the Bénard–von Karman instability. *Phys. Rev. E* **50**, 1.

Hammache, M. & Gharib, M. 1989 A novel method to promote parallel vortex shedding in the wake of circular cylinders. *Phys. Fluids* A **1**, 1611.

Huerre, P. & Monkewitz, P. A. 1990 Local and global instabilities in spatially developing flows. *Ann. Rev. Fluid Mech.* **22**, 473.

Jackson, C. P. 1987 A finite-element study of the onset of vortex shedding in flow past variously shaped bodies. *J. Fluid Mech.* **182**, 23.

Jayaweera, K. O. L. F. & Mason, B. J. 1965 The behaviour of freely falling cylinders and cones in a viscous fluid. *J. Fluid Mech.* **22**, 709.

Karniadakis, G. E. & Triantafyllou, G. S. 1989 Frequency selection and asymptotic states in laminar wakes. *J. Fluid Mech.* **199**, 441.

Karniadakis, G. E. & Triantafyllou, G. S. 1992 The three-dimensional dynamics and transition to turbulence in the wake of bluff objects. *J. Fluid Mech.* **238**, 1.

König, M. 1993 Experimentelle Untersuchung des dreidimensionalen Nachlaufs zylindrischer Körper bei kleinen Reynoldszahlen. *Mitteilungen aus dem Max-Planck-Institut für Strömungsforschung* **111**.

König, M., Eisenlohr, H. & Eckelmann, H. 1990 The fine structure in the Strouhal-Reynolds number relationship of the laminar wake of a circular cylinder. *Phys. Fluids* A **2**, 1607.

König, M., Eisenlohr, H. & Eckelmann, H. 1992 Visualization of the spanwise cellular structure of the laminar wake of wall-bounded circular cylinders. *Phys. Fluids* A **4**, 869.

König, M., Noack, B. R. & Eckelmann, H. 1993 Discrete shedding modes in the von Kármán vortex street. *Phys. Fluids* A **5**, 1846.

Korczak, K. Z. & Patera, A. T. 1986 An isoparametric spectral element method for solution of the Navier–Stokes equation in complex geometry. *J. Comput. Phys.* **62**, 361.

Landau, L. D. & Lifschitz, F. M. 1959 *Fluid Mechanics, Course of Theoretical Physics*, Vol 6. Pergamon Press.

Le Gal, P., Chauve, M. P., Lima, R. & Rezende, J. 1990 Coupled wakes behind two circular cylinders. *Phys. Rev. A* **41**, 4566.

Leweke, T. & Provansal, M. 1995 The flow behind rings: bluff body wakes without end effects. *J. Fluid Mech.* **288**, 265.

Mathis, C. 1983 Propriétés de vitesse transverses dans l'écoulement de Bénard von Kármán aux faibles nombres de Reynolds. Thèse, Université Aix-Marseille III.

Mathis, C., Provansal, M. & Boyer, L. 1987 The Bénard–von Kármán instability: transient and forced regimes. *J. Fluid Mech.* **182**, 1.

Mattingly, G .E. & Criminale, W. O. 1972 The stability of an incompressible two-dimensional wake. *J. Fluid. Mech.* **51**, 233.

Newell, A. C. & Whitehead, J. A. 1969 Finite bandwidth, finite amplitude convection. *J. Fluid Mech.* **38**, 279.

Newhouse, S., Ruelle, D. & Takens, F. 1978 Occurrence of strange axiom A attractors near quasi periodic flows on T^m, $m \geqslant 3$. *Commun. Math. Phys.* **64**, 35.

Noack, B. R. & Eckelmann, H. 1994 A global stability analysis of the steady and periodic cylinder wake. *J. Fluid Mech.* **270**, 297.

Noack, B. R., König, M. & Eckelmann, H. 1993 Three-dimensional stability analysis of the periodic flow around a circular cylinder. *Phys. Fluids* A **5**, 1279.

Olinger, D. J. 1990 Universality in the transition to chaos in open fluid systems. PhD thesis, Yale University.

Olinger, D. J. & Sreenivasan, K. R. 1988 Non linear dynamics of the wake of an oscillating cylinder. *Phys. Rev. Lett.* **60**, 797.

Patera, A. T. 1984 A spectral element method for fluid dynamics: Laminar flow in a channel expansion. *J. Comput. Phys.* **54**, 468.

Peschard, I. 1995 De l'oscillateur aux sillages couplés. Thèse, Université d'Aix-Marseille II.

Roshko, A. 1954 On the development of turbulent wakes from vortex streets. *NACA Rep.* 1191.

Ruelle, D. & Takens, F. 1971 On the nature of turbulence. *Commun. Math. Phys.* **20**, 167.

Sirovich, L. 1985 The Karman vortex trail and flow behind a circular cylinder. *Phys. Fluids* **28**, 2723.

Sreenivasan, K. R. 1985 Transition and turbulence in fluid flows and low-dimensional chaos. In *Frontiers in Fluid Mechanics* (ed. S. H. Davis & J. L. Lumley), pp. 41-67. Springer.

Sreenivasan, K. R., Strykowski, P. J. & Olinger, D. J. 1987 Hopf bifurcation, Landau equation, and vortex shedding behind circular cylinders. *Proc. Forum on Unsteady Flow Separation. ASME Applied Mechanics, Bio engineering and Fluid Engineering Conference, Cincinnati, Ohio, June 11-17,1987*, ASME FED - vol 52,

Strykowski, P. J. & Sreenivasan, K. R. 1990 On the formation and suppression of vortex shedding at low Reynolds numbers. *J. Fluid Mech.* **218**, 71.

Tritton, D. J. 1959 Experiments on the flow past a circular cylinder at low Reynolds numbers. *J. Fluid Mech.* **6**, 547.

Tritton, D. J. 1971 A note on vortex streets behind circular cylinders at low Reynolds numbers. *J. Fluid Mech.* **45**, 203.

Van Atta, C. & Gharib, M. 1987 Ordered and chaotic vortex streets behind cylinders at low Reynolds numbers. *J. Fluid Mech.* **174**, 113.

Wesfreid, J. E., Goujon-Durand, S. & Zielinska, B. J. A. 1995 Global mode behaviour of the streamwise velocity in wakes. *J. Phys. II Paris*, **6**, 1343.

Williamson, C. H. K. 1989 Oblique and parallel modes of vortex shedding in the wake of a circular cylinder at low Reynolds numbers. *J. Fluid Mech.* **206**, 579.

Williamson, C. H. K. 1992 The natural and forced formation of spot-like 'vortex dislocations' in the transition of a wake. *J. Fluid Mech.* **243**, 393.

Williamson, C. H. K. & Prasad, A. 1993 A new mechanism for oblique wave resonance in the 'natural' far wake. *J. Fluid Mech.* **256**, 269.

Zhang, H.-Q., Fey, U., Noack, B. R., König, M. & Eckelmann, H. 1995 On the transition of the cylinder wake, *Phys. Fluids* **7**, 779.